# Dielectric and Viscoelastic Relaxation of Highly Entangled Star Polyisoprene: Quantitative Test of Tube Dilation Model

**Hiroshi Watanabe,* Yumi Matsumiya, and Tadashi Inoue**

*Institute for Chemical Research, Kyoto University, Uji, Kyoto 611-0011, Japan*

*Received October 12, 2001; Revised Manuscript Received December 3, 2001*

ABSTRACT: For highly entangled *cis*-polyisoprene (PI) star polymers having more than 10 entanglements in each arm, dielectric and viscoelastic properties were examined within a context of the generalized tube model incorporating the dynamic tube dilation (DTD) mechanism. The star PI had the type A dipoles parallel along the arm backbone, and the global motion results in the viscoelastic as well as dielectric relaxation. The DTD relationship between the dielectric and viscoelastic relaxation functions $\Phi(t)$ and $\mu(t)$, $\mu(t) \cong [\Phi(t)]^2$ (derived under an assumption of random displacement of the entanglement segment in the dilated tube edge), was not valid for the star PI. Furthermore, the DTD model (Milner−McLeish model) excellently described the viscoelastic data, but considerable differences were found for the dielectric data, even if an effect of the segment displacement in the tube edge was considered in the model. These results indicated a failure of the DTD molecular picture for a few entanglement segments near the branching point. Thus, these segments near the branching point appeared to fully relax via the constraint release (CR) mechanism before the expected tube dilation was completed. On the basis of this result, the DTD model was modified by explicitly incorporating this CR process (though in a crude way). This modification moderately improved the model prediction, suggesting a possible direction of further refinement of the model.

## 1. Introduction

Experiments have established significant differences in the entanglement dynamics of linear and star-branched chains;[1,2] for example, the viscosity $\eta_0$ of linear chains is proportional to the 3.4 power of the molecular weight $M$ while $\eta_0$ of the stars increases exponentially with the arm molecular weight $M_a$. These differences demonstrate that the branching point has a significant effect on the global chain motion.

This effect was nicely captured in an early version of the tube model[3,4] assuming that the star arm is constrained in a fixed tube and the branching point is fixed in space (in the time scale of full relaxation). Under these assumptions, the global relaxation occurs via the arm retraction along the fixed tube. This retraction is associated with an entropic barrier, and the model predictions agree with experiments *if* a parameter value specifying this barrier height is adjusted to $\cong 1/3$ of the value for the Gaussian arms.

However, this adjustment corresponds to a significant reduction of the terminal relaxation time $\tau_{arm}$ of the star arm;[5] for example, the reduction is by a factor of $10^{-5}$ for the star arm having 10 entanglements. In other words, the arm retraction in the fixed tube model (without the parameter adjustment) results in the relaxation much slower than observed.

Ball and McLeish (BM)[5] removed this problem by incorporating the *dynamic tube dilation* (DTD) mechanism in the arm retraction model. In this mechanism, the relaxed portion of the arm behaves as a solvent to dilate the tube and decrease the number $N'$ of stress-sustaining units (with the size being identical to the dilated tube diameter). This decrease of $N'$ reduces the entropic barrier height (by a factor of $1/3$ for the deepest retraction, i.e., for the terminal relaxation).

Thus, the difference between the prediction of the fixed tube model and the measured $\tau_{arm}$ is largely removed in the BM model considering the arm retraction in the dilated tube. Later, Milner and McLeish (MM)[6,7] refined the BM model by considering the Rouse-type thermal fluctuation of the arm length, a refined expression of $\tau_{arm}$ deduced from a solution of the first passage problem, and a refined tube dilation exponent suggested by Colby and Rubinstein,[8] while keeping the essential concept of DTD developed in the BM model. For the linear *viscoelastic* moduli $G^*$ of the star chains, the prediction of the BM and MM models (in particular of the latter) is in excellent agreement with experiments.

The success of these models demonstrates the importance of the DTD mechanism for the star dynamics. However, we should note an important fact that the linear viscoelastic relaxation reflects just a limited aspect of the equilibrium chain motion, i.e., the decay of the orientational anisotropy.[2,9] Thus, the excellent agreement of the DTD predictions and the $G^*$ data does not necessarily guarantee that the actual arm motion coincides with the motion assumed in the models (the retraction along the dilated tube).

Focusing on this problem, we recently examined the dielectric relaxation of star-branched *cis*-polyisoprene (PI) chains.[10,11] The PI chains have so-called type A dipoles[12] parallel along the chain backbone, and their global motion is dielectrically active. For such PI chains, the dielectric and viscoelastic properties detect the same motion in different ways, the former reflecting the orientational correlation of two entanglement segments at separate times ($t$ and 0) while the latter representing the isochronal orientational anisotropy of individual segments.[2,10,11]

In the previous study,[10] we derived an expression of the normalized dielectric relaxation function $\Phi(t)$ in

* To whom correspondence should be addressed.

10.1021/ma011782z CCC: $22.00 
Published on Web 02/16/2002

terms of the average survival fraction of the dilated tube $\varphi'(t)$,

$$\Phi(t) = \varphi'(t) \tag{1}$$

Combining eq 1 with the DTD expression of the normalized relaxation modulus $\mu(t)$ ($=G(t)/G_N$), we obtained a relationship between $\Phi(t)$ and $\mu(t)$ of the PI stars during the DTD process,

$$\mu(t) = [\Phi(t)]^{1+d} \quad \text{with } d = 1-1.3 \tag{2}$$

Here, $d$ is a dilation exponent relating the dilated tube diameter to $\varphi'$.

Equation 1 was derived under assumptions of a minor fluctuation of the branching point and a random displacement of the entanglement segment at the edge of the surviving portion of the dilated tube. As long as these assumptions are valid, eq 2 should hold for the dominant part of the DTD relaxation process. Nevertheless, eq 2 failed for the terminal relaxation of 6-arm PI stars with $M_a \leq 8.1M_e$ ($M_e$ = entanglement spacing).[10] The failure was also found for a series of PI stars having the same $M_a$ ($=7.1M_e$) but different arm numbers $q$ ($=4-15$),[11] confirming that the branching point fluctuation in the dilated tube (suppressed for large $q$) was not the main cause for the observed failure.

The result of the above test suggested that the actual motion of the star arm does not obey the DTD molecular picture at long $t$. However, this test was still incomplete for the following points. First of all, $M_a$ of the PI stars ($\leq 8.1M_e$) used in the test may be still small to examine the validity of the DTD picture in a highly entangled regime. In addition, the assumption of the random segment displacement in the dilated tube edge, utilized in derivation of eq 1, is reasonable at relatively short times but may fail in the long time end of relaxation at $t \sim \tau_{arm}$.

Thus, we have utilized highly entangled PI stars with $M_a > 10M_e$ to further test the DTD picture in relation to the available tube model. In this test, we considered the maximum effect of the displacement of the tube-edge segment on $\Phi(t)$ (tube-edge effect) to modify the expression of $\Phi(t)$. This modified expression was combined with the tube model (MM model) to examine the validity of the DTD picture for the highly entangled stars.

This test revealed significant differences between the dielectric data and the model prediction (with/without the tube-edge effect), although excellent agreement with the viscoelastic data was also noted. This result indicates the failure of the DTD picture for a few entanglement segments near the branching point. This failure is in turn related to a breakdown of the prerequisite for the DTD picture, the rapid equilibration of successive entanglement segments in the dilated tube through their constraint release (CR) motion.[10,11] Thus, the segments near the branching point appear to relax via the CR mechanism before the arm fully retracts along the expected dilated tube. In fact, incorporation of this CR process in the MM model moderately improved the model prediction for the dielectric behavior. Details of these results are presented in this paper.

## 2. Theoretical Section

**2.1. General.** For the monodisperse $q$-arm star chain having the type A dipoles parallel along each arm, the normalized dielectric relaxation function is given by[10]

$$\Phi(t) = \frac{1}{qN_a a^2} \sum_{\alpha,\alpha'=1}^{q} \langle \mathbf{R}_\alpha(t)\cdot\mathbf{R}_{\alpha'}(0)\rangle \quad \text{for } q\text{-arm stars} \tag{3}$$

Here, $\mathbf{R}_\alpha(t)$ indicates a vector starting from the branching point toward the free end of $\alpha$th arm ($\alpha = 1, 2, ..., q$), $a$ is the size of the entanglement segment, and $N_a$ ($=M_a/M_e$) is the number of these segments per each arm. If the branching point is fixed in space (as assumed in the tube models[5-7]), the cross-correlation of different arms vanishes, and eq 3 is simplified to

$$\Phi(t) = \frac{1}{N_a a^2}\langle \mathbf{R}_\alpha(t)\cdot\mathbf{R}_\alpha(0)\rangle \tag{4}$$

(The index $\alpha$ in eq 4 stands for a representative arm.)

The dynamic dielectric constant $\epsilon'$ and dielectric loss $\epsilon''$ at an angular frequency $\omega$ are related to $\Phi(t)$ as[13]

$$\epsilon'(\omega) = \epsilon_\infty - \Delta\epsilon\int_0^\infty \frac{d\Phi(t)}{dt}\cos \omega t \, dt,$$

$$\epsilon''(\omega) = -\Delta\epsilon\int_0^\infty \frac{d\Phi(t)}{dt}\sin \omega t \, dt \tag{5}$$

Here, $\epsilon_\infty$ is the unrelaxed (high-frequency) dielectric constant, and $\Delta\epsilon$ represents the dielectric relaxation intensity for the global chain motion ($\Delta\epsilon = \epsilon_0 - \epsilon_\infty$ with $\epsilon_0$ being the static dielectric constant).

Experimentally, well-entangled star chains exhibit broad distribution of dielectric relaxation modes.[10,14] This distribution can be conveniently expressed in terms of a dielectric relaxation spectrum $\{g_p, \tau_p\}$:

$$\Phi(t) = \sum_{p\geq 1} g_p \exp[-t/\tau_p] \quad (\sum_{p\geq 1} g_p = 1) \tag{6}$$

Here, $g_p$ represents the normalized intensity of the $p$th dielectric mode having the relaxation time $\tau_p$. Correspondingly, $\epsilon'(\omega)$ and $\epsilon''(\omega)$ are also expressed in terms of $\{g_p, \tau_p\}$. The results are conveniently summarized for the normalized dielectric constant $\{\epsilon_0 - \epsilon'(\omega)\}/\Delta\epsilon$ and normalized dielectric loss $\epsilon''(\omega)/\Delta\epsilon$:[10,14]

$$\frac{\epsilon_0 - \epsilon'(\omega)}{\Delta\epsilon} = \omega^2\sum_{p\geq 1} g_p \frac{{\tau_p}^2}{1 + \omega^2{\tau_p}^2},$$

$$\frac{\epsilon''(\omega)}{\Delta\epsilon} = \omega\sum_{p\geq 1} g_p \frac{\tau_p}{1 + \omega^2{\tau_p}^2} \tag{7}$$

**2.2. Expression of $\Phi(t)$ for DTD Process.** Now, we consider the arm motion in the dilated tube to express $\Phi(t)$ in terms of the average survival fraction $\varphi'(t)$ of this tube. We assume the fixed branching point so that this expression can be directly combined with the tube model.[5-7]

In Figure 1, the entanglement segments of the tethered arm at times 0 and $t$ are shown with the filled and unfilled circles, respectively. The dilated tube has the diameter $a' = a\{\varphi'(t)\}^{-d/2}$ with the dilation exponent $d = 1-1.3$, and the surviving portion of this tube (shown with hatching) constrains $\varphi'(t)N_a$ entanglement segments.

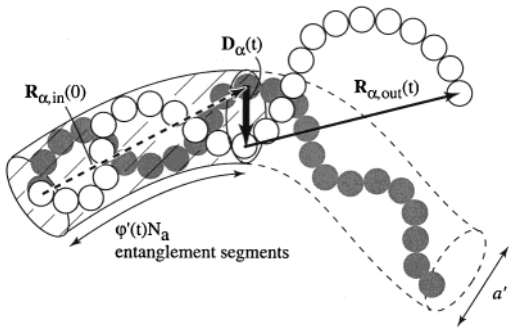


**Figure 1.** Schematic illustration of a star arm in a dilated tube. Filled and unfilled circles indicate the entanglement segments at the times 0 and $t$.

In consideration of the correlation term $\langle \mathbf{R}_\alpha(t)\cdot\mathbf{R}_\alpha(0)\rangle$ appearing in eq 4, the arm contour at the time $t$ is conveniently subdivided in two portions,[10] the outer portion having escaped from the dilated tube and the inner portion remaining in this tube. The end-to-end vector of the outer portion $\mathbf{R}_{\alpha,\mathrm{out}}(t)$ (thin solid arrow in Figure 1) is uncorrelated with the initial arm configuration $\mathbf{R}_\alpha(0)$, and this portion has no contribution to $\Phi(t)$.

The inner portion, composed of $\varphi'(t)N_a$ entanglement segments, contributes to $\Phi(t)$. The end-to-end vector of this portion can be written as $\mathbf{R}_{\alpha,\mathrm{in}}(t) = \mathbf{R}_{\alpha,\mathrm{in}}(0) + \mathbf{D}_\alpha(t)$; cf. Figure 1. Here, $\mathbf{D}_\alpha(t)$ is a displacement vector of the segment in the edge plane of the surviving portion of the dilated tube (thick solid arrow), and $\mathbf{R}_{\alpha,\mathrm{in}}(0)$ is a vector connecting the branching point and this edge segment at the time 0 (thin dotted arrow). Utilizing these vectors, we can rewrite eq 4 as $\Phi(t) = [\langle \mathbf{R}_{\alpha,\mathrm{in}}{}^2(0)\rangle + \langle \mathbf{D}_\alpha(t)\cdot\mathbf{R}_{\alpha,\mathrm{in}}(0)\rangle]/N_a a^2$.

**2.2.1. $\Phi(t)$ in the Absence of the Tube-Edge Effect.** The displacement $\mathbf{D}_\alpha(t)$ would be random and uncorrelated with the initial arm configuration *if* the time scale of our observation is well below a time $\tau_{\mathrm{eq,in}}$ required for equilibration of both length ($|\mathbf{R}_{\alpha,\mathrm{in}}|$) and orientation ($\mathbf{R}_{\alpha,\mathrm{in}}/|\mathbf{R}_{\alpha,\mathrm{in}}|$) of the inner portion. Then, the correlation $\langle \mathbf{D}_\alpha(t)\cdot\mathbf{R}_{\alpha,\mathrm{in}}(0)\rangle$ vanishes to give an expression of $\Phi(t)$:

$$\Phi(t) = \frac{1}{N_a a^2}\langle \mathbf{R}_{\alpha,\mathrm{in}}{}^2(0)\rangle = \varphi'(t) \quad (\text{for } t < \tau_{\mathrm{eq,in}}) \quad (8)$$

This expression was derived previously[10] without specifying the time scale of its validity.

**2.2.2. $\Phi(t)$ in the Presence of the Tube-Edge Effect.** Rigorously speaking, the orientational equilibration of the inner portion of the arm is completed only when the arm fully escapes from the dilated tube. Thus, $\tau_{\mathrm{eq,in}}$ should be close to the longest relaxation time of the arm $\tau_{\mathrm{arm}}$. However, some degree of equilibration may occur even at $t < \tau_{\mathrm{eq,in}}$, and eq 8 may have to be modified accordingly. The largest possible modification is made for a case of full equilibration. For this case, we find

$$\langle \mathbf{D}_\alpha(t)\cdot\mathbf{R}_{\alpha,\mathrm{in}}(0)\rangle = \frac{1}{2}(\langle \mathbf{R}_{\alpha,\mathrm{in}}{}^2(t)\rangle - \langle \mathbf{R}_{\alpha,\mathrm{in}}{}^2(0)\rangle - \langle \mathbf{D}_\alpha{}^2(t)\rangle) = -\frac{1}{2}\langle \mathbf{D}_\alpha{}^2(t)\rangle \quad (9)$$

($\langle\{\mathbf{R}_{\alpha,\mathrm{in}}(t)\}^2\rangle = \langle\{\mathbf{R}_{\alpha,\mathrm{in}}(0)\}^2\rangle$ in the fully equilibrated state.) The mean-square displacement $\langle \mathbf{D}_\alpha{}^2(t)\rangle$ appearing in eq 9 can be evaluated as an integral in the edge plane of the surviving portion of the dilated tube (designated as a $\xi-\eta$ plane),

$$\langle \mathbf{D}_\alpha{}^2(t)\rangle = \frac{1}{\pi^2(a'/2)^4}\int\{(\xi-\xi_0)^2 + (\eta-\eta_0)^2\}\mathrm{d}\xi\,\mathrm{d}\xi_0\,\mathrm{d}\eta\,\mathrm{d}\eta_0 = \left(\frac{a'-a}{2}\right)^2 \quad (10)$$

Here, $(\xi, \eta)$ and $(\xi_0, \eta_0)$ indicate the coordinates of the edge segment at the times $t$ and 0, and the integral is conducted in the region available for the center of mass of this segment (= a circular region of the diameter $a' - a$). The displacement vanishes when the tube is not dilated.

From eqs 9 and 10 together with the expression of the dilated tube diameter $a' = a\{\varphi'(t)\}^{-d/2}$, $\Phi(t) = [\langle \mathbf{R}_{\alpha,\mathrm{in}}{}^2(0)\rangle + \langle \mathbf{D}_\alpha(t)\cdot\mathbf{R}_{\alpha,\mathrm{in}}(0)\rangle]/N_a a^2$ can be rewritten as

$$\Phi(t) = \varphi'(t) - \frac{1}{8N_a}[\{\varphi'(t)\}^{-d/2} - 1]^2 \quad (d = 1-1.3) \quad (11)$$

Some comments need to be added for this expression of $\Phi(t)$. In eq 11, the second term represents the *tube-edge effect*, i.e., the dielectric relaxation due only to the segment displacement in the tube-edge plane. This effect is overestimated in eq 11 because the equilibration assumed in eqs 9 and 11 is completed only at $t \sim \tau_{\mathrm{arm}}$. Thus, eq 11 gives the $\Phi(t)$ for the case of the maximum tube-edge effect. As noted from eq 11, this effect becomes important at long $t$ where $\varphi'(t)$ decays to $O(N_a{}^{-1/(1+d)})$, thereby giving comparable magnitudes of the $\varphi'$ and $\{\varphi'\}^{-d}/N_a$ factors.

**2.2.3. DTD Relationship in the Presence of the Tube-Edge Effect.** The displacement of the tube-edge segment introduces no significant change in the DTD expression of the normalized modulus, $\mu(t) = \{\varphi'(t)\}^{1+d}$, for the dominant part of the arm relaxation.[5−7,10] Thus, the DTD relationship between $\mu(t)$ and $\Phi(t)$ of the star chains, being modified for the tube-edge effect (cf. eq 11), can be written as

$$\Phi(t) = \{\mu(t)\}^{1/(1+d)} - \frac{1}{8N_a}[\{\mu(t)\}^{-d/2(1+d)} - 1]^2 \quad (12)$$

The difference between the DTD relationships without and with the tube-edge effect (eqs 2 and 12) becomes important at long $t$ where $\mu(t) \sim O(1/N_a)$. Experiments[1,2] indicate that the steady-state compliance $J_e$ of well-entangled star chains is close to the Rouse−Ham compliance, $J_{RH} = 2(15q-14)M/5(3q-2)^2cRT \cong 2N_a/3G_N$ (for the arm number $q \geq 6$). Thus, the normalized terminal relaxation intensity $\mu(\tau_{\mathrm{arm}})$ scales as $1/G_N J_e \sim 1/G_N J_{RH} = 3/2N_a$, suggesting that the tube-edge effect becomes important at long $t \sim O(\tau_{\mathrm{arm}})$ where $\mu(t)$ decays to $O(1/N_a)$.

In general, the displacement of the branching point may also induce the dielectric relaxation at long $t \sim O(\tau_{\mathrm{arm}})$. However, for the test of the DTD picture within the context of the tube model, we limit ourselves to the case of fixed branching point assumed in the model.

**2.2. DTD Models.** The Ball−McLeish (BM) and Milner−McLeish (MM) models consider that the entanglement segment at the curvilinear coordinate $z$ (= curvilinear length measured from the free arm end) has a well-defined relaxation time $\tau(z)$. For the BM

model, this $\tau(z)$ is given by[5]

$$\tau_{BM}(z) = \tau^* \exp\left[\frac{U_{BM}(z)}{k_B T}\right]$$
$$\text{with } U_{BM}(z) = \frac{15}{8} N_a k_B T\left[\frac{z^2}{{L_{eq}}^2} - \frac{2z^3}{3{L_{eq}}^3}\right] \quad (13)$$

Here, $L_{eq}$ ($=N_a a$) denotes the equilibrium arm length, $k_B$ is the Boltzmann constant, $T$ is the absolute temperature, and $\tau^*$ corresponds to the Rouse relaxation time within one entanglement segment. (This $\tau^*$ specifies a short time cutoff of the model.)

For the more elaborated MM model considering both shallow and deep retraction processes (with the former being equivalent to Rouse-type fluctuation of the arm length), $\tau(z)$ is written as[6,7]

$$\tau_{MM}(z) \cong \frac{\tau_{sh}(z) \exp\left(\frac{U_{MM}(z)}{k_B T}\right)}{1 + \frac{\tau_{sh}(z)}{\tau_{dp}(z)} \exp\left(\frac{U_{MM}(z)}{k_B T}\right)} \quad (14)$$

Here, $\tau_{sh}(z)$ and $\tau_{dp}(z)$ are the characteristic times for the shallow and deep retraction processes,

$$\tau_{sh}(z) = \frac{225\pi^3 \tau^* {N_a}^4}{256}\left(\frac{z}{L_{eq}}\right)^4 \quad (15)$$

and

$$\tau_{dp}(z) \cong \frac{\tau^* {N_a}^{3/2} \pi^{5/2} \exp\left(\frac{U_{MM}(z)}{k_B T}\right)}{30^{1/2}\left(\frac{z}{L_{eq}}\right)\left[\left\{1 - \frac{z}{L_{eq}}\right\}^{2d} + \Gamma\left(\frac{1}{d+1}\right)^{-2}\left(\frac{4+4d}{15N_a}\right)^{2d(d+1)}\right]^{1/2}} \quad (16)$$

with

$$U_{MM}(z) = \frac{15 N_a k_B T}{4(d+1)(d+2)}\left[1 - \left(1 - \frac{z}{L_{eq}}\right)^{d+1}\left(1 + \frac{(d+1)z}{L_{eq}}\right)\right] \quad (d = {}^4/_3) \quad (17)$$

For both models, the normalized relaxation modulus is written in a form[5-7]

$$\mu(t) = \frac{d+1}{L_{eq}} \int_0^{L_{eq}} \left[1 - \frac{z}{L_{eq}}\right]^d \exp\left(-\frac{t}{\tau(z)}\right) dz \quad (18)$$

where $d = 1$ (for the BM model) and/or $d = {}^4/_3$ (for the MM model). The displacement of the tube-edge segment introduces no significant change in this expression of $\mu(t)$.

Now, we formulate the dielectric $\Phi(t)$ for the BM and MM models in the presence of the tube-edge effect. For a given retraction distance $z$, the dielectric memory $\tilde{\Phi}(z)$ is evaluated as the $\Phi$ given by eq 11 with $\varphi'$ being replaced by $1 - z/L_{eq}$. Consequently, the dielectric memory sustained by the entanglement segments at the coordinates between $z$ and $z + dz$ can be expressed as

$$d|\tilde{\Phi}| = \left[1 + \frac{d}{8N_a}\left\{\left(1 - \frac{z}{L_{eq}}\right)^{-(d+1)} - \left(1 - \frac{z}{L_{eq}}\right)^{-(1+d/2)}\right\}\right]\frac{dz}{L_{eq}} \quad (19)$$

This memory decays with the relaxation time, $\tau(z) = \tau_{BM}(z)$ and/or $\tau_{MM}(z)$ (cf. eqs 13 and 14). Thus, in the presence of the maximum tube-edge effect, the $\Phi(t)$ formulated for the BM and MM models is written as

$$\Phi(t) = \frac{1}{K_n L_{eq}} \int_0^{z_c} [1 + \Xi(z)] \exp\left(-\frac{t}{\tau(z)}\right) dz \quad (20)$$

with

$$\Xi(z) = \frac{d}{8N_a}\left\{\left(1 - \frac{z}{L_{eq}}\right)^{-(d+1)} - \left(1 - \frac{z}{L_{eq}}\right)^{-(1+d/2)}\right\} \quad (21a)$$

and

$$z_c = L_{eq} - a \quad \text{and}$$
$$K_n = \frac{z_c}{L_{eq}} + \frac{1}{8N_a}\left[1 - \left(1 - \frac{z_c}{L_{eq}}\right)^{-d/2}\right]^2 \quad (21b)$$

In eq 20, the upper bound of the integral $z_c$ is introduced to avoid a divergence of the integral. (The full relaxation can be achieved when the arm retracts by a distance $L_{eq} - a$, and this distance is chosen as $z_c$; cf. eq 21b.) The $K_n$ is a normalization factor ensuring $\Phi(0) = 1$. Note that the $\Phi(t)$ in absence of the tube-edge effect is given by eq 20 with $\Xi(z) = 0$, $z_c = L_{eq}$, and $K_n = 1$.[10]

The longest dielectric relaxation time deduced from the MM model is given by $\tau_{MM}(L_{eq})$ in absence of the tube-edge effect and by $\tau_{MM}(z_c)$ in the presence of this effect. For large $N_a$ (>10), the $\tau_{MM}(L_{eq})$ and $\tau_{MM}(z_c)$ are close to each other, and the tube-edge effect just results in a change of the dielectric mode distribution to enhance the terminal relaxation intensity.

## 3. Experimental Section

**3.1. Materials.** Two *cis*-polyisoprene (PI) star samples were anionically synthesized in high vacuum at room temperature. *sec*-Butyllithium and heptane were utilized as the initiator and solvent, respectively. For comparison, two linear PI samples were also synthesized anionically.

The PI star arms have the type A dipoles parallel along the arm backbone, and these dipoles are once inverted at the branching point. The linear PI chains have the noninverted type A dipoles. These star/linear samples were freeze-dried from benzene solutions containing an antioxidant, butylhydroxytoluene (~0.1 wt % to the samples), sealed in Ar atmosphere, and stored in a deep freezer until use.

In the star synthesis, an aliquot of the PI anions was recovered for characterization of the arm. The remaining anions were allowed to react with a hexafunctional coupler, bis(trichloromethylsilyl)ethane. The concentration of this coupler was set to be ~90% equimolar to the anions (to ensure the full coupling). The crude product of the coupling reaction was thoroughly fractionated from benzene/methanol mixtures to remove the excess (unreacted) arms and recover the monodisperse 6-arm star PI samples.

The star and linear PI samples were characterized with GPC (CO-8020 and DP-8020, Tosoh) combined with a law-angle laser light scattering (LALS) photometer (LS-8000, Tosoh). The eluent was THF, and monodisperse linear PI samples[10,15,16] were utilized as the elution standards. The

**Table 1. Characteristics of 6-Arm Star and Linear PI Samples**[a]

| $10^{-3}M_w$[b] | $M_w/M_n$[c] | $10^{-3}M_a$ (for star PI)[c] |
|---|---|---|
| 6-Arm Star PI | | |
| 354 | 1.05 | 59.0 |
| 459 | 1.06 | 80.1 |
| Linear PI | | |
| 180 | 1.06 | |
| 308 | 1.08 | |

[a] Cis:trans:vinyl ≅ 75:20:5 for PI synthesized with *sec*-butyllithium in heptane. [b] Determined from LALS combined with GPC. [c] Determined from elution calibration of GPC. (LALS-GPC analysis gave $M_w/M_n$ values smaller than those shown in Table 1.)

molecular weight and polydispersity index of these samples are summarized in Table 1. The number of entanglements in each star arm is $N_a = M_a/M_e \cong 12$ and 16; namely, the star samples have more than 10 entanglements in each arm and are highly entangled in the bulk state. The linear PI samples are even more heavily entangled ($N = M/M_e = 36$ and 62).

**3.2. Measurements.** For the bulk PI samples (Table 1), linear viscoelastic measurements were carried out with a laboratory rheometer (ARES, Rheometrics) in a parallel plate geometry with the plate diameter of 2.5 cm. The time−temperature superposition worked well at temperatures $T = 0-70$ °C, and the storage and loss moduli $G'$ and $G''$ were reduced at 40 °C.

For the highly entangled PI samples utilized in this study, the terminal dielectric relaxation was too slow to be detected with the transformer bridge (TB) method. Thus, we combined the TB method and an adsorption current (AdC) method to measure the dynamic dielectric constant $\epsilon'$ and dielectric loss $\epsilon''$ in the entire relaxation domain for the global motion, as described below. The $\epsilon'$ and $\epsilon''$ data thus obtained at $T = 0-70$ °C were found to obey the time−temperature superposition with the shift factor $a_T$ being identical to that for the viscoelastic data. These dielectric data were reduced at 40 °C.

**TB Method.** The TB method was utilized at relatively short times (high frequencies) where the relaxational response due to the chain motion overwhelmed the direct current (dc) conductance due to ionic impurities. In this method, the PI sample was charged in a guarded parallel plate cell with a vacant capacity $C_0 = 120$ pF and subjected to a sinusoidally oscillating electric field (of the amplitude $E_0 < 10$ V/mm) at various angular frequencies, $\omega/s^{-1} = 6 \times 10^2 - 1 \times 10^6$. The resulting sinusoidal current was compensated with a transformer bridge (1620A, QuadTech) by tuning the capacitance $C$ and conductance $G$ of this bridge. From these $C$ and $G$ values, $\epsilon'$ and $\epsilon''$ of the sample were obtained as

$$\epsilon'(\omega) = C(\omega)/C_0, \quad \epsilon''(\omega) = G(\omega)/C_0\omega \tag{22}$$

**AdC Method.** The AdC method, similar to that developed by Hayakawa et al.[17] and Adachi et al.,[18] was utilized at long times where the dc conductance was not negligible. In this method, the sample was charged in the same dielectric cell as utilized in the TB method and subjected to an oscillatory rectangular voltage (of the amplitude $V_0 = 27$ and/or 18 V) generated with a homemade circuit (cf. Figure 2a). The polarity of the voltage was periodically switched with a function generator (WF1944, NF Corp.), and the resulting current $I(t)$ was measured with an electrometer (TR8411, Advantest) and stored in a digital recorder (DL708G, Yokogawa).

The stationary changes of the rectangular voltage $V(t)$ and current $I(t)$ with the time $t$ are schematically shown in Figure 2b. This $V(t)$ is decomposed into its Fourier components as

$$V(t) = V_0 \sum_{p=\text{odd}} \frac{4}{p\pi} \sin \omega_p t \quad \text{with } \omega_p = \frac{p\pi}{t_0} \tag{23}$$

where $\omega_p$ is a frequency of the $p$th component determined by the half-period $t_0$ of the rectangular voltage. The corresponding current $I(t)$ is a sum of the relaxational current $I_{relax}(t)$ due to the chain motion in the sample and the dc current $I_{dc}$ due to ionic impurities; cf. Figure 2b. The $I_{relax}(t)$, given by a convolution of the electric field ($\propto V$) and $\Phi$, is compactly written as

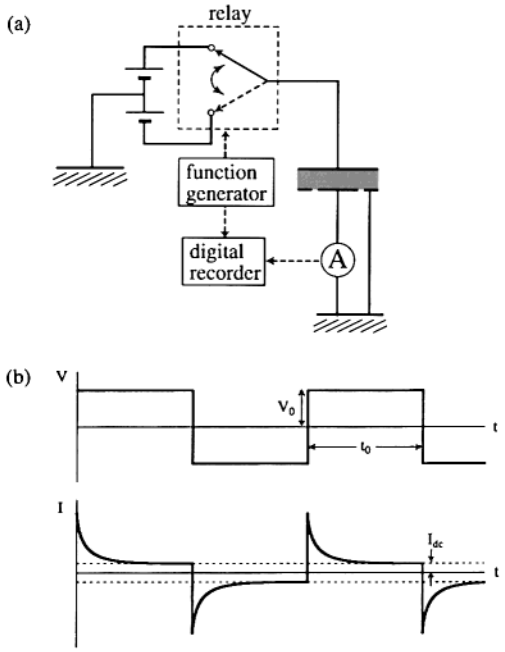


**Figure 2.** (a) Schematic illustration of a circuit for dielectric measurements with the adsorption current method. (b) Schematic illustration of the voltage ($V$) and current ($I$) signals measured with this method. $I_{dc}$ is a dc current due to ionic impurities.

$$I_{relax}(t) = \frac{4V_0C_0}{t_0}\left(\epsilon_\infty \sum_{p=\text{odd}} \cos \omega_p t - \Delta\epsilon \int_0^\infty \frac{d\Phi(t')}{dt'} \sum_{p=\text{odd}} \cos \omega_p (t - t')\, dt'\right) \tag{24}$$

As noted from eqs 5 and 24, $\epsilon'$ and $\epsilon''$ are obtained as the Fourier integral of $I_{relax}(t)$:

$$\epsilon'(\omega_p) = \frac{1}{2V_0C_0}\int_0^{t_0} I_{relax}(t) \cos \omega_p t\, dt, \quad \epsilon''(\omega_p) = \frac{1}{2V_0C_0}\int_0^{t_0} I_{relax}(t) \sin \omega_p t\, dt \tag{25}$$

In the actual measurements, the half-period $t_0$ was chosen to be 6−10 times longer than the terminal viscoelastic relaxation time $\langle\tau_G\rangle_w$ so that the dielectric relaxation of the PI sample was completed within the time $t_0$. The $I(t)$ signal was accumulated/averaged over 32 periods to reduce electrical noises. Typical $I(t)$ data obtained under these conditions are shown in Figure 3 (unfilled circles; $t_0 = 80$ s and $\langle\tau_G\rangle_w = 8$ s). With this choice of $t_0$, the $I_{dc}$ value is accurately determined as the time-independent $I$ value at long $t$. The $I_{relax}$ (filled circles) obtained by subtracting this $I_{dc}$ from the $I(t)$ data was integrated according to eq 25 to obtain $\epsilon'$ and $\epsilon''$.

This integration was limited to $t > 0.1$ s where the response of our circuit (Figure 2a) accurately followed the dielectric change in the material. (For $t < 0.1$ s, a delay in the circuit was not negligible.) Consequently, the $\epsilon'$ obtained by this integration does not include the instantaneous response (characterized by $\epsilon_\infty$) and thus corresponds to $\epsilon' - \epsilon_\infty$. Since the dielectric loss is not contributed from the instantaneous response, the limitation of the integration range ($t > 0.1$ s) did not introduce any significant uncertainty in $\epsilon''$ (eq 25).

With the above choice of $t_0$ ($= 6\langle\tau_G\rangle_w - 10\langle\tau_G\rangle_w$), the $I_{relax}$ (almost) completely decays to zero within the time $t_0$ and practically coincides with $2V_0C_0\Delta\epsilon\{-d\Phi(t)/dt\}$; cf. eqs 5 and

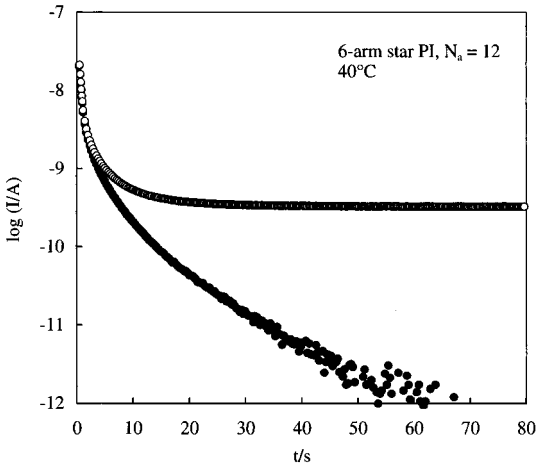


**Figure 3.** Semilogarithmic plots of the adsorption current data obtained for a PI star ($N_a = 12$) at 40 °C. The half period of the rectangular voltage is $t_0 = 80$ s. Unfilled circles indicate the raw $I(t)$ data, and the filled circles represent the relaxational current $I_{relax}(t)$ obtained by subtracting the dc current from the $I(t)$ data.

25. This $I_{relax}$ can be expressed in terms of the dielectric relaxation times $\tau_p$ and intensities $g_p$ as (cf. eq 6)

$$I_{relax}(t) = 2V_0C_0\Delta\epsilon\sum_{p\geq 1}\frac{g_p}{\tau_p}\exp[-t/\tau_p] = Q_{relax}\sum_{p\geq 1}\frac{g_p}{\tau_p}\exp[-t/\tau_p] \quad (26)$$

with

$$Q_{relax} = \int_0^{t_0} I_{relax}(t)\,dt \quad (27)$$

In derivation of eq 26, we have utilized a relationship $\sum_p g_p = 1$ (eq 6) and regarded the $t_0$ in eq 27 to be practically infinite (because the $\exp[-t/\tau_p]$ terms included in $I_{relax}$ (eq 26) almost fully decay to zero within $t_0$).

On the basis of eq 26, the measured $I_{relax}(t)/Q_{relax}$ ratio was decomposed into exponentially decaying modes to evaluate $\tau_p$ and $g_p$ (for $p \leq 8$). At low $\omega$, the $\epsilon'$ and $\epsilon''$ calculated from these $\tau_p$ and $g_p$ (eq 7) agreed well with those obtained from the Fourier integration (eq 25). Thus, we utilized the $\epsilon'$ and $\epsilon''$ obtained from this analysis of the $I_{relax}(t)/Q_{relax}$ ratio together with those obtained from eq 25.

## 4. Results and Discussion

**4.1. Overview.** Figure 4 shows the normalized dielectric constant $\{\epsilon_0 - \epsilon'\}/\Delta\epsilon$ and dielectric loss $\epsilon''/\Delta\epsilon$ of the 6-arm PI stars in the well-entangled regime. For comparison, the dielectric behavior of monodisperse linear PI chains (having noninverted type A dipoles) is shown in Figure 5. The data for the stars with $N_a = 12$ and 16 and the linear PI with $N = 36$ and 62 were obtained in this study, and the other data were obtained in the previous studies.[10,15,16]

As noted from Figures 4 and 5, our dielectric test covers a low-$\omega$ range comparable to that examined in typical viscoelastic tests. The adsorption current method enabled us to cover such low $\omega$ where the highly entangled star/linear PI chains exhibited the terminal dielectric relaxation.

At our reference temperature, 40 °C, the local (or segmental) relaxation of PI chains emerges at $\omega > 10^7$ $s^{-1}$.[16,19] Thus, the dielectric relaxation observed in Figures 4 and 5 is exclusively attributed to the global motion of the star/linear PI chains. At sufficiently low $\omega$, these chains exhibit the terminal tails, $\{\epsilon_0 - \epsilon'\} \propto \omega^2$ and $\epsilon'' \propto \omega$, that characterize the completion of the global dielectric relaxation. From these tails, we evaluated the second-moment average relaxation time:

$$\langle\tau_\epsilon\rangle_w = \frac{[\{\epsilon_0 - \epsilon'(\omega)\}/\omega^2]_{\omega\to 0}}{[\epsilon''(\omega)/\omega]_{\omega\to 0}} = \frac{\sum_{p\geq 1} g_p\tau_p^{\,2}}{\sum_{p\geq 1} g_p\tau_p} \quad (28)$$

This $\langle\tau_\epsilon\rangle_w$ is related to the dielectric spectrum $\{g_p, \tau_p\}$ in a well-defined way shown in eq 28 and close to the longest dielectric relaxation time.[10,14] In fact, $\langle\tau_\epsilon\rangle_w$ is analogous to the viscoelastic terminal relaxation time $\langle\tau_G\rangle_w$ that is evaluated from the viscosity $\eta_0$ (= $[G''/\omega]_{\omega\to 0}$) and compliance $J_e$ (= $[G'/G'')^2]_{\omega\to 0}$) and related

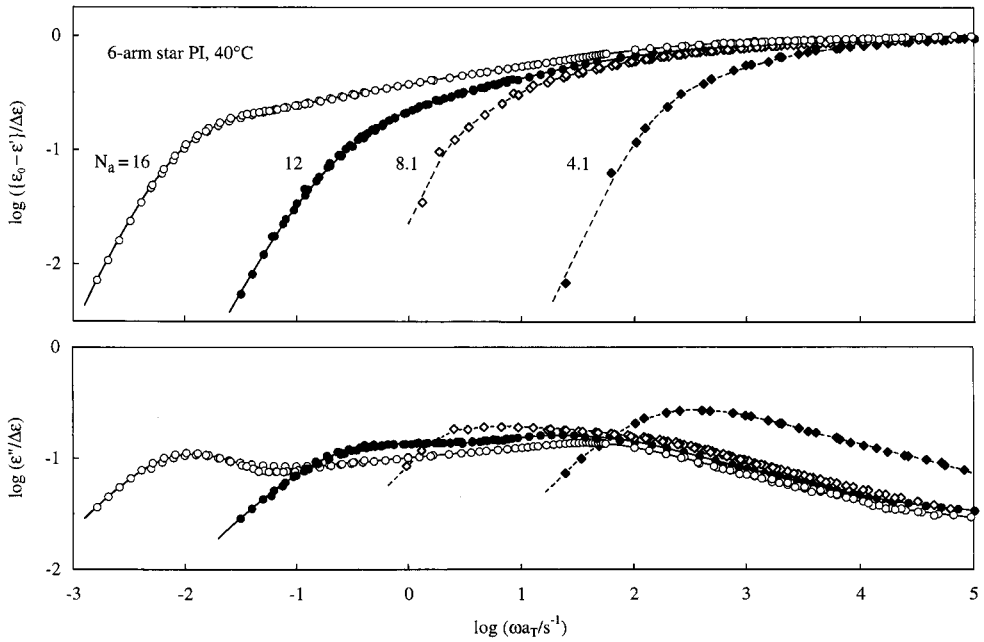


**Figure 4.** Normalized dielectric constant $\{\epsilon_0 - \epsilon'\}/\Delta\epsilon$ and dielectric loss $\epsilon''/\Delta\epsilon$ at 40 °C measured for 6-arm PI stars in the well-entangled regime. These PI stars have the type A dipoles once inverted at the branching point.

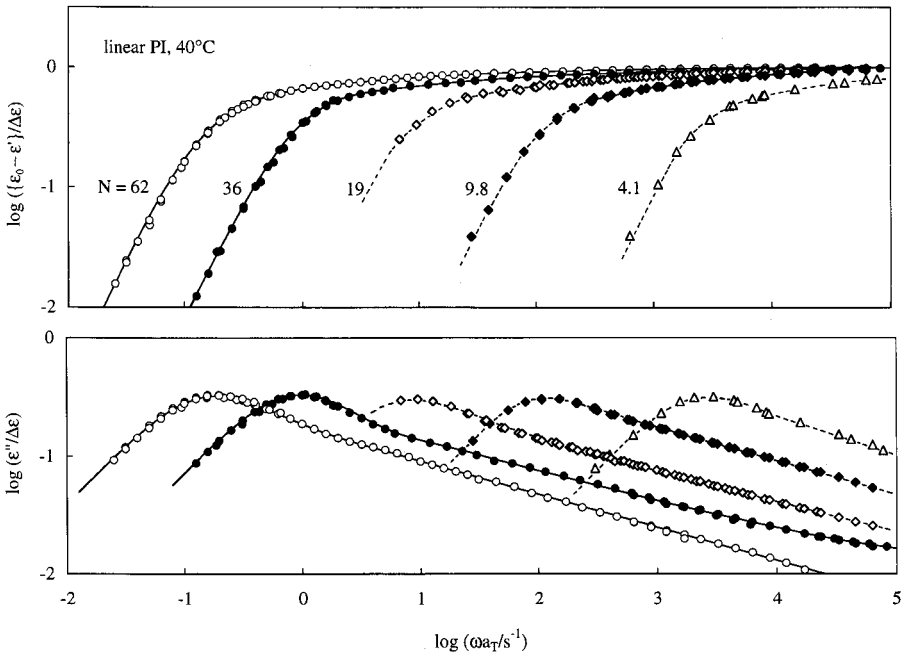


**Figure 5.** Normalized dielectric constant $\{\epsilon_0 - \epsilon'\}/\Delta\epsilon$ and dielectric loss $\epsilon''/\Delta\epsilon$ at 40 °C measured for linear PI chains in the well-entangled regime. These linear PI chains have the noninverted type A dipoles.

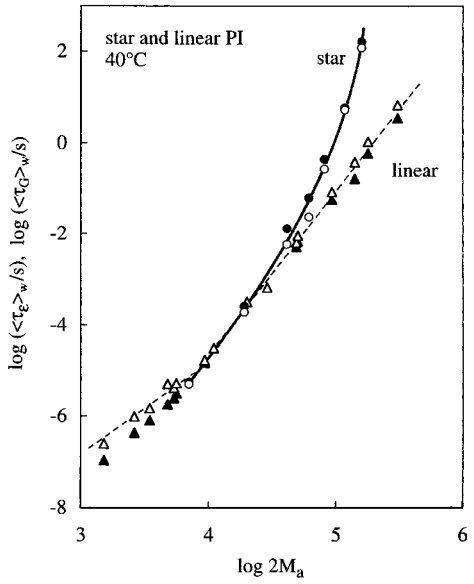


**Figure 6.** Dielectric and viscoelastic terminal relaxation times, $\langle\tau_\epsilon\rangle_w$ (unfilled symbols) and $\langle\tau_G\rangle_w$ (filled symbols) at 40 °C, plotted against the span molecular weight $2M_a$ (for PI stars) and/or the total molecular weight $M$ (for linear PI chains).

to the viscoelastic spectrum $H(\tau)$ (expressed in a continuous form),[1,2]

$$\langle\tau_G\rangle_w = J_e\eta_0 = \frac{\int_{-\infty}^{\infty} H(\tau)\tau^2 \, d \ln \tau}{\int_{-\infty}^{\infty} H(\tau)\tau \, d \ln \tau} \qquad (29)$$

For the well-entangled PI chains examined in Figures 4 and 5, Figure 6 shows plots of $\langle\tau_\epsilon\rangle_w$ (unfilled symbols) and $\langle\tau_G\rangle_w$ (filled symbols) against the span molecular weight $2M_a$ (for the star PI) and/or the total molecular weight $M$ (for the linear PI). The $\eta_0$ and $J_e$ data of these chains (utilized in the evaluation of $\langle\tau_G\rangle_w$) are summarized in Table 2. For comparison, Figure 6 also shows

**Table 2. Zero-Shear Viscosity $\eta_0$ and Steady-State Compliance $J_e$ at 40 °C Measured for the 6-Arm Star and Linear PI Chains Examined in Figures 4 and 5**

| $10^{-3}M$ or $10^{-3}M_a$ | $\log(\eta_0/\text{Pa s})$ | $\log(J_e/\text{Pa}^{-1})$ |
|---|---|---|
| | 6-Arm Star PI | |
| 20.5[a] | 3.11 | −4.97 |
| 40.7[a] | 4.27 | −4.62 |
| 59.0[a] | 5.31 | −4.48 |
| 80.1[a] | 6.44 | −4.26 |
| | Linear PI | |
| 20.5[b] | 1.64 | −5.12 |
| 48.8[b] | 2.97 | −5.26 |
| 94.0[b] | 4.02 | −5.28 |
| 180[b] | 5.01 | −5.23 |
| 308[b] | 5.81 | −5.25 |

[a] Arm molecular weight. [b] Total molecular weight.

the terminal relaxation times of lightly entangled/unentangled PI chains examined in the previous studies.[10,15,16,19−21] For both star and linear PI chains, $\langle\tau_\epsilon\rangle_w$ and $\langle\tau_G\rangle_w$ are close to each other. This result confirms that the viscoelastic and dielectric relaxation processes detect the same global motion of the chains.

Figures 4−6 clearly demonstrate differences in the dielectric behavior of the star and linear chains. As seen in Figure 6, $\langle\tau_\epsilon\rangle_w$ of the entangled linear chains increases in proportion to $M^{3.5\pm0.1}$ while the entangled stars exhibit much stronger, exponential $M_a$ dependence of $\langle\tau_\epsilon\rangle_w$. (This difference has been well-known for the viscoelastic $\langle\tau_G\rangle_w$.[1−7,22] This study confirms the same difference for the dielectric $\langle\tau_\epsilon\rangle_w$ in the well-entangled regime.)

A more important difference of the linear and star chains is noted for the dielectric mode distribution reflected in the $\omega$ dependence of $\{\epsilon_0 - \epsilon'\}/\Delta\epsilon$ and $\epsilon''/\Delta\epsilon$. For the linear PI chains, this distribution is insensitive to $N$; see Figure 5. This $N$ insensitivity is similar to that known for the viscoelastic mode distribution in the well-entangled regime.[1,2]

In contrast, the dielectric mode distribution of the star PI chains broadens significantly with increasing $N_a$; see Figure 4. In particular, the stars with $N_a \geq 12$ exhibit

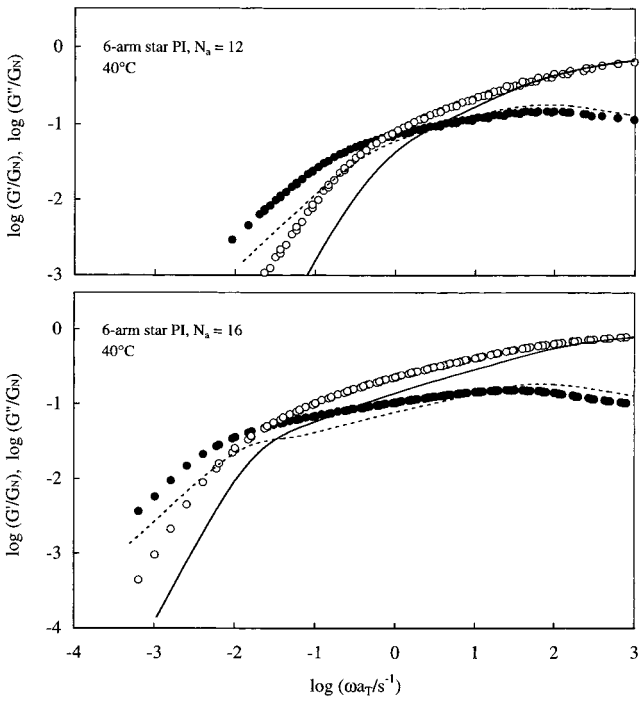


**Figure 7.** Test of the simplest DTD relationship (eq 2; derived in absence of the tube-edge effect) for highly entangled PI stars at 40 °C. The normalized moduli data, $G'/G_N$ (unfilled circles) and $G''/G_N$ (filled circles) with $G_N = 4.8 \times 10^5$ Pa, are compared with the moduli (curves) calculated from the dielectric data through this relationship.

two broad peaks of $\epsilon''$. This result indicates the existence of a dielectric relaxation process much faster than the terminal relaxation process. Viscoelastic $G''$ of highly entangled stars exhibits a similar high-$\omega$ peak[2,22] (with an example seen later in Figure 7), and this peak has been assigned to the Rouse-type thermal fluctuation of the arm length. Thus, the fast dielectric process resulting in the $\epsilon''$ peak at $\omega a_T = 50-100$ s$^{-1}$ (for $N_a = 12$ and 16) can be also attributed to this fluctuation. With decreasing $N_a$, the terminal relaxation process is significantly accelerated (cf. Figure 6) to reduce the separation between the fast and terminal relaxation processes. Thus, for the star PI with $N_a = 8.1$, the fast fluctuation process does not give a well-resolved $\epsilon''$ peak but is observed as a shoulder in the $\epsilon''$ curve at $\omega a_T \cong 200$ s$^{-1}$; cf. Figure 4. For the shortest star with $N_a = 4.1$, the two processes merge with each other to give a single broad $\epsilon''$ peak at $\omega a_T \cong 400$ s$^{-1}$.

The $\epsilon''$ peak/shoulder assigned to the arm length fluctuation shifts to lower $\omega$ with increasing $N_a$; see Figure 4. This shift is quantitatively consistent with the $N_a^{-2.6}$ dependence reported for the $G''$ peak frequency.[22]

Differing from this fluctuation process, the terminal viscoelastic/dielectric relaxation of the entangled stars is exponentially retarded with increasing $N_a$; cf. Figure 6. On the basis of the excellent agreement of the tube model prediction and viscoelastic data,[6,7] one might assign this exponentially slowing terminal relaxation to the *full* retraction of the star arm along the dilated tube (cf. eqs 13 and 14). However, our test of the DTD picture utilizing both viscoelastic and dielectric data poses a question for this assignment. The results of this test are presented in the remaining part of this paper.

**4.2. Test of DTD Relationship in the Absence of the Tube-Edge Effect.** The DTD relationship derived in absence of the tube-edge effect,[10] eq 2, can be easily tested for the star PI chains. If these chains obey eq 2 with the smallest possible dilation exponent $d = 1$, their normalized moduli should be related to the dielectric spectrum $\{g_p, \tau_p\}$ as[10]

$$\frac{G'(\omega)}{G_N} = \omega^2 \sum_{p,k\geq 1} \frac{h_{pk}\tau_{pk}^2}{1+\omega^2\tau_{pk}^2}, \quad \frac{G''(\omega)}{G_N} = \omega \sum_{p,k\geq 1} \frac{h_{pk}\tau_{pk}}{1+\omega^2\tau_{pk}^2} \quad \text{(for DTD with } d = 1\text{)} \quad (30)$$

with

$$h_{pk} = g_p g_k \quad \text{and} \quad \tau_{pk} = [\tau_p^{-1} + \tau_k^{-1}]^{-1} \quad (31)$$

For a given dielectric $\Phi(t)$, eqs 30 and 31 specify the slowest possible viscoelastic DTD relaxation. (For the general cases of $d > 1$, the viscoelastic relaxation is faster than that for $d = 1$; cf. eq 2.)

We utilized the dielectric data shown in Figure 4 to evaluate the dielectric spectrum of the highly entangled star PI with a previously reported iteration method.[16] Some details of this method and a merit of the use of the spectrum in our test of the DTD picture (eq 30) are explained in Appendix A.

In Figure 7, the $G'/G_N$ and $G''/G_N$ calculated from this spectrum are shown with the solid and dotted curves. These calculated moduli are close to the $G'/G_N$ and $G''/G_N$ data (unfilled and filled circles; $G_N = 4.8 \times 10^5$ Pa) at high $\omega a_T > 10$ s$^{-1}$ where the $G''$ peak attributable to the arm length fluctuation is observed. However, at lower $\omega$, considerable differences are noted for the measured and calculated moduli. Specifically, the viscoelastic DTD relaxation calculated from the dielectric data is *faster* than observed. Since the dilation exponent utilized in the calculation ($d = 1$) gives the slowest possible DTD relaxation, this result allows us to conclude the failure of the DTD picture (in absence of the tube-edge effect) at long times where the highly entangled PI stars exhibit the terminal relaxation. This failure was observed also for less entangled star PI.[10,11]

Equation 2 should hold also for the monodisperse linear PI chains if the DTD picture is valid for these chain.[14,15] Utilizing the dielectric data shown in Figure 5, we calculated the moduli for the DTD process to test this picture for the highly entangled linear PI chains ($N = 32$ and 64). The results are shown in Figure 8. The DTD predictions (curves) are close to the measured moduli (circles), meaning that the DTD picture holds as a very good approximation for the highly entangled linear PI chains. This success of the DTD picture was found also for less entangled linear PI.[15]

The difference between the star and linear PI chains, the failure and success of the DTD picture, can be related to the prerequisite for the DTD process. Since the tube dilates as a result of the mutual equilibration of successive entanglement segments through their constraint release (CR) motion,[2,10,11] the DTD picture is valid only at times longer than the CR equilibration time $\tau^{**}$.

In the previous study,[11] we estimated $\tau^{**}$ for moderately entangled star/linear PI chains to test this DTD criterion. In this study, we made the same test for the highly entangled PI chains and found that the criterion is satisfied in the terminal regime for the linear chains but violated for the star chains. This failure of the DTD

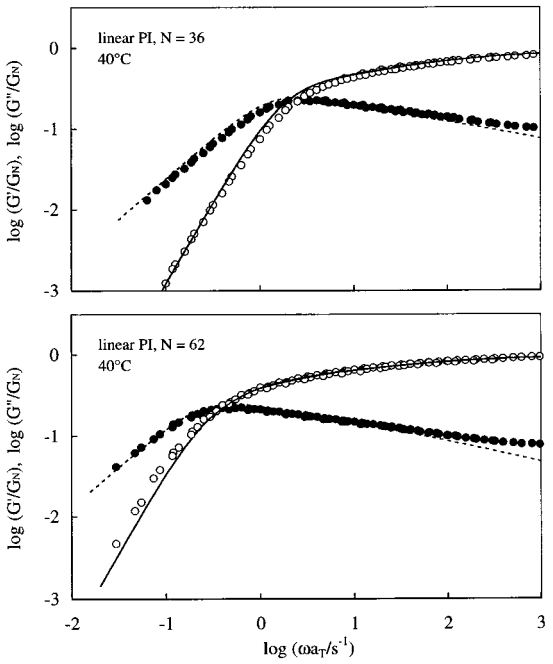


**Figure 8.** Test of the simplest DTD relationship (eq 2; derived in absence of the tube-edge effect) for highly entangled linear PI chains at 40 °C. The normalized moduli data, $G'/G_N$ (unfilled circles) and $G''/G_N$ (filled circles) with $G_N = 4.8 \times 10^5$ Pa, are compared with the moduli (curves) calculated from the dielectric data through this relationship.

picture for the star chains is related to the broad distribution of the motional modes of these chains, while the validity found for the linear chains reflects their narrow mode distribution.[11] Details of these results are summarized in Appendix B.

**4.3. Comparison of Data with the DTD Model in the Absence of the Tube-Edge Effect.** The simplest DTD picture (eq 2) fails for the highly entangled PI stars, as demonstrated in Figure 7. Here, we utilize the BM/MM models (in absence of the tube-edge effect) to further test this picture.

The normalized moduli $G'/G_N$ and $G''/G_N$ of these models are calculated as the Fourier transformation of $\mu(t)$ given by eq 18. For the highly entangled PI stars with $N_a = 12$ and 16, respectively, the top panels of Figures 9 and 10 compare the moduli data (circles) with the MM prediction (solid curves). For the star with $N_a = 12$, the data are also compared with the BM prediction in the top panel of Figure 11. In the calculation, we allowed the $N_a$ value to be adjusted a little ($N_{a,cal} = 15$ and 20 instead of $N_a = 12$ and 16) to achieve the best agreement of the calculated and measured moduli. This adjustment is comparable, in magnitude, to uncertainties in the experimental $M_a$ and $G_N$ values utilized in the calculation of $N_a$ ($= M_a G_N/\rho RT$; $\rho$ = density). In fact, the adjustment of similar magnitude was made in previous studies.[5−7]

The remaining model parameter, $\tau^*$ (cf. eqs 13−16), was determined in a way that the BM/MM models (with the above $N_{a,cal}$ values) reproduced the viscosity $\eta_0$ of the PI stars. As noted in the top panels of Figures 9−11, the models with this choice of $\tau^*$ excellently describe the moduli data in the dominant part of the terminal relaxation ($\omega a_T < 100$ s$^{-1}$); compare the solid curves and circles. In particular, the MM model excellently reproduces the $G''$ peak (at $\omega a_T = 10-100$ s$^{-1}$) attributable to the Rouse fluctuation of the star arm length. Similar

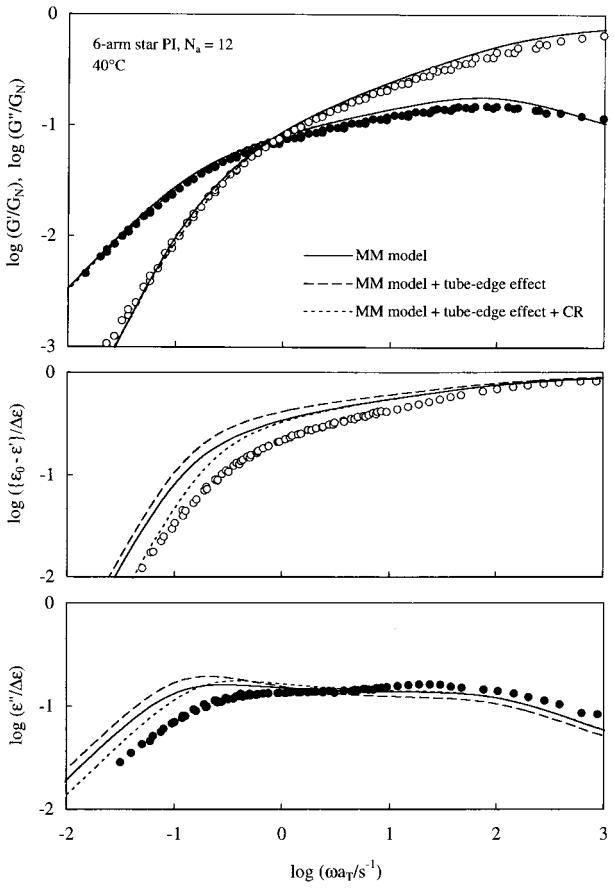


**Figure 9.** Comparison of viscoelastic/dielectric data (circles) of PI star ($N_a = 12$) with predictions of the MM model in absence of the tube-edge effect (solid curves). Dashed curves indicate the prediction of the model combined with the tube-edge effect. Dotted curves represent the prediction of the DTD-CR model (= MM model modified through incorporation of the CR process). For further details, see text.

agreement between the viscoelastic data and models was demonstrated previously.[5−7]

The dielectric $\Phi(t)$ formulated for the MM model in absence of the tube-edge effect is given by eq 20 with $\Xi = 0$, $z_c = L_{eq}$, and $K_n = 1$. The model predictions for $\{\epsilon_0 - \epsilon'\}/\Delta\epsilon$ and $\epsilon''/\Delta\epsilon$ of the PI stars, calculated as the Fourier transformation of this $\Phi(t)$, are shown with the solid curves in the middle and bottom panels of Figures 9 and 10. The values of the model parameters ($N_{a,cal}$ and $\tau^*$) are the same as those giving the excellent agreement between the calculated and measured moduli (top panels). Nevertheless, the calculated $\{\epsilon_0 - \epsilon'\}/\Delta\epsilon$ and $\epsilon''/\Delta\epsilon$ are considerably different from the data in the terminal regime, although the model fairly well describes the high-$\omega$ $\epsilon''$ peak attributable to the Rouse-type fluctuation of the arm length.

The BM predictions for $\{\epsilon_0 - \epsilon'\}/\Delta\epsilon$ and $\epsilon''/\Delta\epsilon$, calculated in a similar way, are shown with the solid curves in the bottom panel of Figure 11. Differences between the model and experiments are noted not only in the terminal regime but also in the Rouse fluctuation regime. The high-$\omega$ $\epsilon''$ peak, reproduced by the MM model, is not predicted from the BM model. Correspondingly, the BM model does not describe the $G''$ peak at $\omega a_T = 50-100$ s$^{-1}$ reproduced by the MM model; see the top panel of Figure 11. (These differences between the BM and MM models reflect the lack of the Rouse fluctuation mechanism in the former, as explained in more details in Appendix C.)

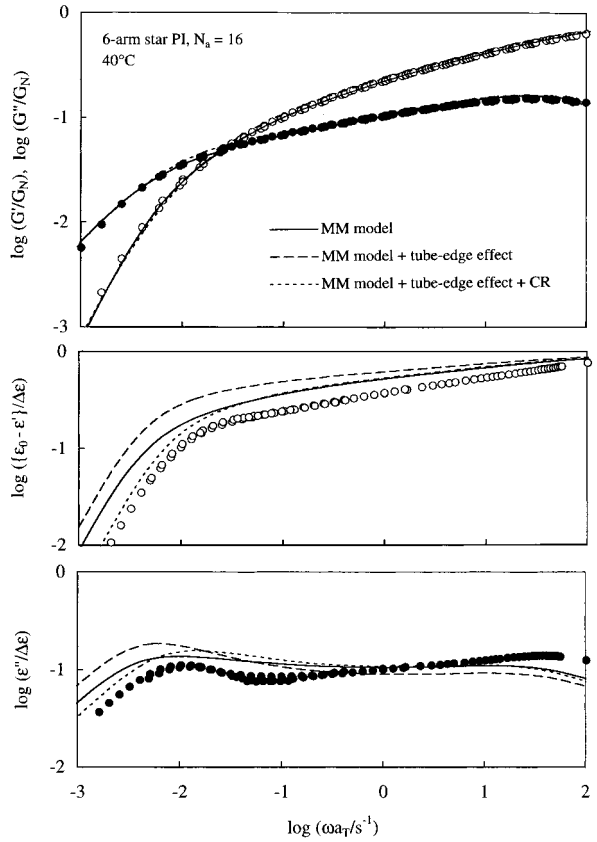


**Figure 10.** Comparison of viscoelastic/dielectric data (circles) of PI star ($N_a$ = 16) with predictions of the MM model in absence of the tube-edge effect (solid curves). Dashed curves indicate the prediction of the model combined with the tube-edge effect. Dotted curves represent the prediction of the DTD-CR model (= MM model modified through incorporation of the CR process). For further details, see text.

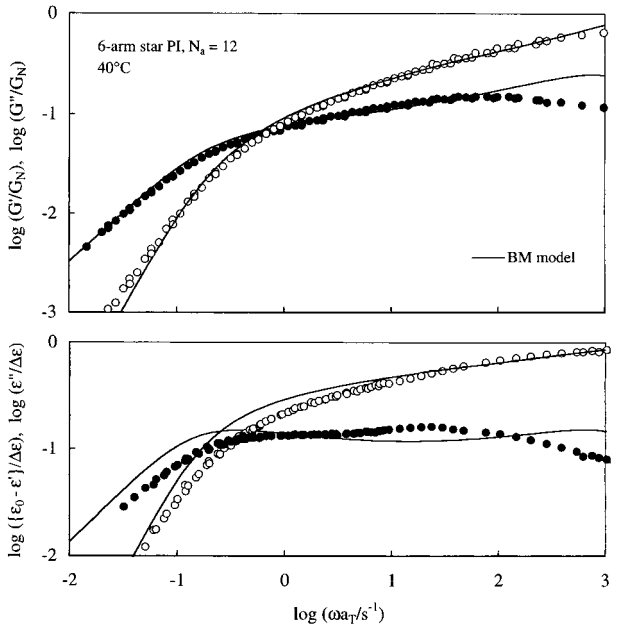


**Figure 11.** Comparison of viscoelastic and dielectric data (circles) of PI star ($N_a$ = 12) with predictions of the BM model (solid curves).

It should be emphasized that both BM and MM models predict the dielectric terminal relaxation *slower* than observed if the model parameters ($N_{a,cal}$ and $\tau^*$) are chosen to excellently reproduce the moduli data; see Figures 9−11. Concerning this point, we examined the models with nonadjusted $N_a$ but found no better agreement with the dielectric data. Thus, the deviation between the dielectric data and model prediction is not due to the small adjustment of $N_a$.

In Figure 7, we have demonstrated that the viscoelastic DTD relaxation calculated from the dielectric data is faster than observed. Consequently, the dielectric relaxation calculated from the viscoelastic data through the DTD relationship (eq 2) is slower than observed. This result is in harmony with that seen in Figures 9−11. In particular, in absence of the tube-edge effect, the $\mu(t)$ of the MM model is numerically close to $[\Phi(t)]^2$ in the entire range of $t$, although the rigorous DTD relationship for this model is given by $\mu(t) = [\Phi(t)]^{1+d} = [\Phi(t)]^{7/3}$ at short $t$; see Appendix C. Thus, the result seen in Figure 7 (the failure of the simplest DTD relationship) is almost equivalent to those observed in Figures 9 and 10.

**4.4. Comparison of Data with the DTD Model in the Presence of the Tube-Edge Effect.** For the highly entangled PI stars, the previous sections confirmed the failure of the DTD picture in the absence of the tube-edge effect. However, we should remember that the DTD relationship (eq 2) is modified when the tube-edge effect on $\Phi(t)$ is considered. Thus, the validity of the DTD picture needs to be also tested in the presence of this effect. Here, this test is made through comparison of the data of the PI stars with the predictions of the MM model combined with the tube-edge effect. (The MM model is utilized in this test because this model can describe the Rouse fluctuation of the arm length.)

For the largest possible displacement of the segment in the tube edge, the $\Phi(t)$ formulated for the MM model is given by eqs 20 and 21 (with $d = {}^4/_3$). This displacement induces no significant change in the expression of $\mu(t)$ (eq 18). Thus, in the calculation of $\{\epsilon_0 - \epsilon'\}/\Delta\epsilon$ and $\epsilon''/\Delta\epsilon$ in the presence of the tube-edge effect, we chose the parameters ($N_{a,cal}$ and $\tau^*$) giving the best agreement between the moduli data and the MM prediction without this effect (cf. top panels of Figures 9 and 10). The dielectric behavior thus calculated is shown with the dashed curves in the middle and bottom panels of Figures 9 and 10. Since eq 20 is formulated for the maximum tube-edge effect, these dashed curves would overestimate this effect. (Thus, the dielectric curve calculated from the MM model with a realistic magnitude of the tube-edge effect should be between the dashed and solid curves.)

As noted in Figures 9 and 10, the tube-edge effect moderately increases the terminal dielectric intensity to give a well-resolved $\epsilon''/\Delta\epsilon$ peak at low $\omega$, because the displacement of the edge segment is larger in a more dilated tube at longer $t$; compare the dashed and solid curves. However, for large $N_a$ (>10), the calculated terminal relaxation time does not change with this effect, as explained earlier for eq 20. Thus, the dielectric relaxation calculated in the presence of the tube-edge effect is still slower than observed.

From this result as well as those demonstrated in the pervious sections, we can conclude that the PI star arm does not retract along the fully dilated tube (with the diameter $a' = a\{\Phi(t)\}^{-d/2}$) at long $t$. This failure of the DTD picture (either with or without the tube-edge effect) suggests an important contribution of the constraint release (CR) mechanism to the terminal dynamics of the star chains, as pointed out also in the previous studies.[10,11]

Here, we need to add a comment about the DTD relationship for the linear chains modified for the tube-edge effect. This modified relationship is cast in a form similar to that shown in eq 12 (with the $1/8N_a$ factor being replaced by $1/4N$;[23] $N$ = number of entanglement segments in the linear chain). Thus, in principle, the tube-edge effect changes the DTD relationship between $\mu$ and $\Phi$ of the linear chains. However, for the chains with $N \gg 1$, the terminal viscoelastic modes have a considerably narrow distribution and $\mu(t)$ does not significantly decay up to $t = \langle\tau_G\rangle_w$. For this case, the correction due to the tube-edge effect, having the order of $\mu(t)^{-d/(1+d)}/N$ (cf. second term in eq 12), is negligible in the entire range of $t$ up to $\langle\tau_G\rangle_w$. For this reason, the DTD relationship without this effect is valid for the highly entangled linear chains, as observed in Figure 8.

**4.5. Effect of Terminal CR Relaxation.** The DTD picture is valid in a time scale $t$ longer than the CR equilibration time. In the MM model, each segment has the relaxation time $\tau_{MM}(z)$ determined by its coordinate $z$ (cf. eq 14), and the tube diameter dilates to $a' = a(1 - z/L_{eq})^{-2/3}$ at $t = \tau_{MM}(z)$. This dilation is equivalent to the CR equilibration of successive $(1 - z/L_{eq})^{-4/3}$ segments. Thus, the DTD formulation in this model is valid for the segments having $\tau_{MM}(z) > \tau^{**}(z)$, but a modification is required for those having $\tau_{MM}(z) < \tau^{**}(z)$, where $\tau^{**}(z)$ is the CR equilibration time of the $(1 - z/L_{eq})^{-4/3}$ segments.

Following this argument, we estimated the threshold coordinate $z^{**}$ specifying the crossover from the DTD picture ($z < z^{**}$) to the CR picture ($z > z^{**}$) and attempted to modify the MM model by explicitly incorporating the CR process for the segments at $z > z^{**}$. Features of this modified model and the results of the comparison with experiments are summarized below.

*4.5.1. Estimation of DTD-CR Crossover Threshold.* Graessley formulated the *local* entanglement lifetime $t_w$ for a linear chain as a mean waiting time for the first removal of the constraint due to motion of surrounding linear chains:[24] $t_w = \int_0^\infty \{F(t)\}^{n_g}\,dt$ where $F(t)$ is an appropriate relaxation function (that coincides with the tube survival fraction in the Graessley model) and $n_g$ denotes the number of constraints per each entanglement point.

In the above DTD-CR crossover molecular picture for the star arm, the first removal of the constraint for a given entanglement segment occurs through two modes: If the entangling partner (a segment in the other arm) has the coordinate $z' < z^{**}$, the removal would be dominated by the MM-type arm retraction. On the other hand, if the partner has $z' > z^{**}$, the removal can occur at the time $t_w$ through the CR motion of this partner. Applying the Graessley formulation to this dual-mode removal, we may estimate the $t_w$ for the star arm as

$$t_w = \int_0^\infty \{F(t)\}^{n_g}\,dt \quad \text{with } F(t) = \frac{1}{L_{eq}}\int_0^{z^{**}} \exp\left(-\frac{t}{\tau_{MM}(z')}\right) dz' + \left\{1 - \frac{z^{**}}{L_{eq}}\right\} \exp\left(-\frac{t}{t_w}\right) \tag{32}$$

For a given $z^{**}$ value, the $t_w$ is numerically calculated from eq 32, and the CR equilibration time $\tau^{**}$ is evaluated from this $t_w$. If the chosen $z^{**}$ is the correct DTD-CR threshold, this $\tau^{**}$ should coincide with $\tau_{MM}(z^{**})$. On the basis of this argument, the threshold can be determined from a comparison of $\tau^{**}$ and $\tau_{MM}$ described below.

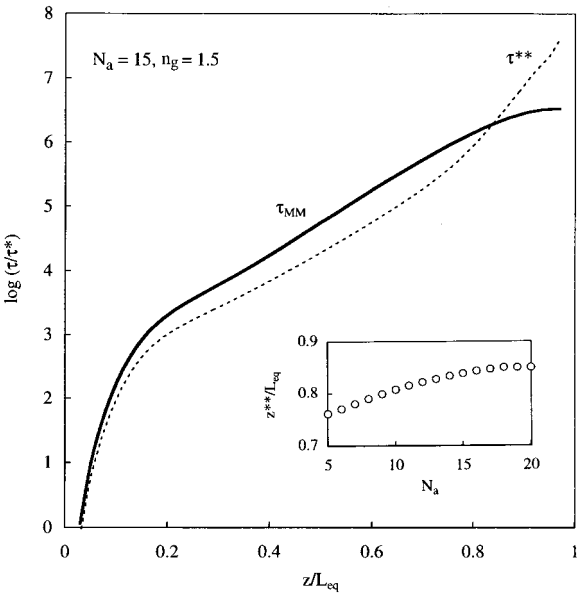


**Figure 12.** Comparison of the relaxation time $\tau_{MM}(z)$ of an entanglement segment at a curvilinear coordinate $z$ deduced from the MM model (solid curve) with the time $\tau^{**}(z)$ required for CR equilibration over $(1 - z/L_{eq})^{-4/3}$ segments (dashed curve). Both $\tau_{MM}(z)$ and $\tau^{**}(z)$ are normalized by $\tau^*$ (Rouse relaxation time in one segment) and plotted against the reduced coordinate $z/L_{eq}$. The DTD-CR crossover threshold $z^{**}$ is evaluated as the coordinate where the $\tau_{MM}(z)$ and $\tau^{**}(z)$ curves cross each other. The $N_a$ dependence of this $z^{**}$ is shown in the inserted panel. For further details, see text.

The characteristic times of the actual CR process are close to those predicted from the Rouse-CR model.[2,24] In this model, an effective friction coefficient for the *local CR hopping* of the entanglement segment is given by $12k_BTt_w/a^2$. Thus, for a given retraction distance $z$, the time $\tau^{**}$ required for the *full dilation* of the tube to the diameter $a' = a(1 - z/L_{eq})^{-2/3}$ can be estimated as an orientational Rouse equilibration time:

$$\tau^{**}(z) = \frac{t_w}{2}\sin^{-2}\left(\frac{\pi}{2\beta}\right) \quad \text{with } \beta = \frac{1}{(1 - z/L_{eq})^{4/3}} \tag{33}$$

Here, $\beta$ is the number of successive entanglement segments that should be equilibrated for the full dilation to occur. (The expression of $\tau^{**}$ (eq 33), being derived on the basis of the discretized Rouse dynamics,[1,2] is applicable in the entire range of $\beta$ ($\geq$1). For large $\beta$, eq 33 is reduced to the continuous Rouse-CR expression utilized in Appendix C.)

For the stars of various $N_a$, we calculated $\tau^{**}(z)$ from eqs 32 and 33 (with $z^{**}$ in eq 32 being replaced by $z$) and estimated the DTD-CR threshold $z^{**}$ by comparing this $\tau^{**}(z)$ with $\tau_{MM}(z)$ (eq 14). The results for $N_a = 15$ and $n_g = 1.5$ are shown in Figure 12, where $\tau^{**}(z)$ and $\tau_{MM}(z)$ are plotted against a reduced coordinate $z/L_{eq}$. The threshold, $z^{**} = 0.84L_{eq}$, is evaluated as the coordinate where the $\tau^{**}(z)$ and $\tau_{MM}(z)$ curves cross each other. For $z > z^{**}$, $\tau^{**}(z)$ is longer than $\tau_{MM}(z)$, and the CR equilibration (prerequisite for DTD) does not occur in time.

The DTD-CR threshold $z^{**}$ evaluated in this way increases gradually with $N_a$; see the inset in Figure 12. However, in a practically accessible range of $N_a$ (<20), $z^{**}$ remains considerably smaller than $L_{eq}$. Thus, a

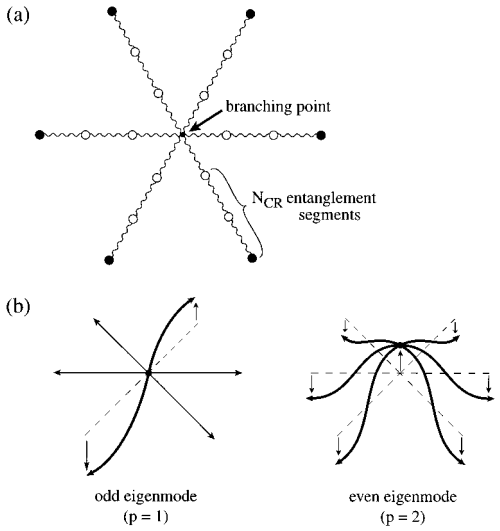


**Figure 13.** (a) Schematic illustration of a 6-arm Rouse−Ham chain (branched bead−spring chain). (b) Schematic illustration of odd and even eigenmodes of this chain. For the star chain having the dipoles (thick arrows) inverted at the branching point, all odd eigenmodes and a subset of even eigenmodes (having the mode indices = twice of even integers) are dielectrically inert.

nonnegligible number of segments near the branching point appear to relax at long $t$ through the CR motion, not through the full arm retraction along the dilated tube.

Of course, the $z^{**}$ value changes with the chosen $n_g$ value and the method of estimating $t_w$ (eq 32). In addition, the distribution of the entanglement lifetime, having a delicate effect on the CR dynamics,[11] may also affect the $z^{**}$ value. However, irrespective of these details, the insufficient CR equilibration (= failure of the DTD picture) for large $z$ seems to be concluded from the comparison of $\tau_{MM}$ and $\tau^{**}$.

Thus, in this study, we utilize the $z^{**}$ values shown in Figure 12 (that gave the terminal dielectric relaxation time close to the data) to modify the MM model by simply incorporating the CR process for $z > z^{**}$. The aim of this crude modification is to examine the importance of the CR mechanism in the star dynamics and explore a direction of the model refinement.

*4.5.2. CR Relaxation Process.* The branching point largely moves during the CR process for the segments at $z > z^{**}$. The Rouse−Ham (RH) model[2,25,26] allowing this motion can be utilized to formulate the viscoelastic $\mu_{CR}(t)$ and dielectric $\Phi_{CR}(t)$ for this CR process. These $\mu_{CR}(t)$ and $\Phi_{CR}(t)$ are defined as the *normalized* relaxation functions satisfying $\mu_{CR}(0) = \Phi_{CR}(0) = 1$.

The RH model describes the stochastic motion of a bead−spring star chain having a frictionless branching point; see Figure 13a. The arm is composed of $N_{CR}$ beads each having an effective friction coefficient $\zeta_{eff}$. For the CR process of our interest, the beads (the motional unit in the RH model) correspond to the entanglement segments at $z \geq z^{**}$ (DTD-CR threshold), not the dilated segments of the size $a' > a$. Thus, the bead number $N_{CR}$ (= spring number) and the spring constant $\kappa$ are given by

$$N_{CR} = N_a\left(1 - \frac{z^{**}}{L_{eq}}\right) \quad \text{and} \quad \kappa = \frac{3k_BT}{a^2} \tag{34}$$

with $z^{**}$ being evaluated in Figure 12. Since this $N_{CR}$ was not very large (<4 for the PI stars examined in Figures 9 and 10), we solved the discretized RH equation of motion to calculate $\mu_{CR}(t)$ and $\Phi_{CR}(t)$. The coefficient $\zeta_{eff}$ included in these $\mu_{CR}(t)$ and $\Phi_{CR}(t)$ is specified later in relation to the chain motion during the terminal CR process.

In the RH model for the monodisperse $q$-arm star chain, the eigenmodes of motion are classified into two series;[25−27] see Figure 13b. In the odd eigenmodes, the branching point does not move, and the antisymmetric, synchronized motion is activated for a pair of arms. Thus, the odd modes for a given relaxation time has a degeneracy of $q - 1$.[25,26] In contrast, the even eigenmodes induce the displacement of the branching point and activate the symmetric, synchronized motion of all $q$ arms. These even modes are not degenerated.

These RH eigenmodes were utilized to calculate $\mu_{CR}(t)$ and $\Phi_{CR}(t)$:

$$\mu_{CR}(t) = \frac{1}{qN_{CR}}\left[\sum_{p=1}^{N_{CR}}(q-1)\exp\left(-\frac{2t}{\tau_{2p-1}^{(CR)}}\right) + \sum_{p=1}^{N_{CR}}\exp\left(-\frac{2t}{\tau_{2p}^{(CR)}}\right)\right] \tag{35}$$

and

$$\Phi_{CR}(t) = \frac{1}{K_{CR}}\sum_{p=\text{odd}\leq N_{CR}}\sin^{-2}\left(\frac{p\pi}{2N_{CR}}\right)\exp\left(-\frac{t}{\tau_{2p}^{(CR)}}\right) \tag{36}$$

with

$$K_{CR} = \sum_{p=\text{odd}\leq N_{CR}}\sin^{-2}\left(\frac{p\pi}{2N_{CR}}\right) \tag{37}$$

The eigenmode relaxation times $\tau_{2p-1}^{(CR)}$ and $\tau_{2p}^{(CR)}$ appearing in eqs 35 and 36 are given by

$$\tau_{2p-1}^{(CR)} = \frac{\zeta_{eff}}{4\kappa}\sin^{-2}\left(\frac{\{2p-1\}\pi}{2\{2N_{CR}+1\}}\right) \quad \text{for odd modes } (p = 1, 2, ..., N_{CR}) \tag{38}$$

$$\tau_{2p}^{(CR)} = \frac{\zeta_{eff}}{4\kappa}\sin^{-2}\left(\frac{p\pi}{2N_{CR}}\right) \quad \text{for even modes } (p = 1, 2, ..., N_{CR}) \tag{39}$$

The $\Phi_{CR}$ detects the orientational correlation at the times $t$ and 0 and (cf. eq 3), while $\mu_{CR}$ reflects the orientational anisotropy at respective $t$.[2,10,11,28,29] Thus, for the incoherent CR process,[28,29] $\Phi_{CR}$ and $\mu_{CR}$ include the first-order and second-order moment averages of the eigenmode amplitudes at the time $t$. For this reason, the dielectric modes decay as $\exp\{-t/\tau_\alpha^{(CR)}\}$ with $\tau_\alpha^{(CR)}$ being the CR eigenmode relaxation time ($1 \leq \alpha \leq 2N_{CR}$) while the viscoelastic modes decay as $\exp\{-2t/\tau_\alpha^{(CR)}\}$; see eqs 35 and 36.

It should be also noted that $\Phi_{CR}(t)$ is contributed only from a subset of even eigenmodes having the mode indices equal to twice of odd integers; see eq 36. This *dielectric extinction* of some eigenmodes reflects the dipole inversion at the branching point:[26] Because of this inversion, the odd eigenmodes do not change the total polarization of the chain and are dielectrically inert; see

Figure 13b. The even eigenmodes with the mode indices equal to twice of even integers are also inert because these modes activate the same displacements for the arm end and branching point, thereby inducing no change in the polarization of the arm. (Of course, all eigenmodes contribute to the viscoelastic $\mu_{CR}$ (eq 35) irrespective of the dipole inversion.)

Even with the inverted dipoles, the dielectric extinction does not occur if the motion of the $q$ arms is not synchronized and not described as a sum of the eigenmodes. From this point of view, the extinction can be regarded as a characteristic feature of the RH-type CR process.

*4.5.3. Effective Friction for Full CR Relaxation.* The motional unit considered in the terminal CR process (eqs 35 and 36) is the entanglement segment of the size $a$, not the coarse-grained (dilated) segment considered in the DTD process. The effective friction coefficient $\zeta_{eff}$ specifies an average hopping rate of this unit during the terminal CR process.

The friction coefficient defined for the *local* CR hopping over the distance $a$ is written as $\zeta^{(local)} = 4\kappa t_w$ ($= 12k_BTt_w/a^2$),[2,24] where $t_w$ is the local entanglement lifetime (eq 32). The corresponding longest relaxation time $\tau_1$ is calculated from eq 38 with $p = 1$ and $\zeta_{eff} = \zeta^{(local)}$:

$$\tau_1\{\zeta^{(local)}\} = t_w \sin^{-2}\left(\frac{\pi}{2\{2N_{CR}+1\}}\right) \qquad (40)$$

However, for the terminal CR relaxation to occur, the $N_{CR}$-th segments (shown with the filled circles in Figure 13a) need to hop over a distance $N_{CR}^{-1/2}a$. This hopping is allowed only after the arm retracts over the distance $z^{**}$ to release these segments, namely, only at $t > \tau_{MM}(z^{**})$. The $\tau_1$ for this retraction-determined CR hopping process can be calculated by remodeling the RH arm (Figure 13a) as an arm composed of only one end segment that is bound to the branching point through a spring of the strength $\kappa' = \kappa/N_{CR}$: The friction coefficient $\zeta^{(ret)}$ for that hopping process is given by $4\kappa'\tau_{MM}(z^{**})$, and the corresponding $\tau_1$ is obtained from eq 38 with $N_{CR} = 1$, $p = 1$, and $\kappa$ and $\zeta_{eff}$ being replaced by $\kappa'$ and $\zeta^{(ret)}$:

$$\tau_1\{\zeta^{(ret)}\} = 4\tau_{MM}(z^{**}) \qquad (41)$$

The prefactor of 4 appearing in eq 41 reflects a fact that the terminal CR relaxation requires the antisymmetric motion of *two* end segments.

The $\tau_1\{\zeta^{(ret)}\}$ is different from $\tau_1\{\zeta^{(local)}\}$; cf. eqs 40 and 41. This difference suggests that the entanglement lifetime has a distribution determined by the length scale (and direction) of the CR hopping. The lifetime for the local hopping over the distance $a$ is given by $t_w$ (eq 32), and the tube should dilate as a result of the accumulation of such local hopping processes (in both radial and axial directions of the tube). However, the terminal CR process requires a larger scale hopping (predominantly in the axial direction of the dilated tube at $t = \tau_{MM}(z^{**})$), and the entanglement lifetime assigned to each segment during this process should be different from $t_w$.

The effective friction coefficient $\zeta_{eff}$ (included in eqs 38 and 39) is determined according to this distribution of the lifetime. The accumulation of the local CR hopping processes leads to the terminal CR relaxation, and this accumulation requires the time $\tau_1\{\zeta^{(local)}\}$. Thus, if $\tau_1\{\zeta^{(local)}\} > \tau_1\{\zeta^{(ret)}\}$, this relaxation should occur at $\tau_1\{\zeta^{(local)}\}$. For this case, we can equate $\tau_1\{\zeta^{(local)}\}$ and $\tau_1^{(CR)}$ (eq 38) to obtain $\zeta_{eff} = 4\kappa t_w$ ($= \zeta^{(local)}$).

On the other hand, if $\tau_1\{\zeta^{(ret)}\} > \tau_1\{\zeta^{(local)}\}$, the terminal CR relaxation rate should be determined by the arm retraction over the distance $z^{**}$. For this case, we can equate $\tau_1\{\zeta^{(ret)}\}$ and $\tau_1^{(CR)}$ to evaluate $\zeta_{eff}$ as

$$\zeta_{eff} = 16\kappa\tau_{MM}(z^{**}) \sin^2\left(\frac{\pi}{2\{2N_{CR}+1\}}\right) \qquad (42)$$

(This situation is similar to that for a pom-pom chain:[30] the trunk of this chain relaxes only after the relaxation of the arms attached to the trunk ends is completed, and the friction factor for the trunk is determined by the arms.)

For the highly entangled PI stars with $N_a = 12$ and 16 (cf. Figures 9 and 10), the DTD-CR threshold $z^{**}$ shown in Figure 12 was utilized to calculate $\tau_1\{\zeta^{(local)}\}$ and $\tau_1\{\zeta^{(ret)}\}$ (cf. eqs 14, 32, 40, and 41). For these stars, we found $\tau_1\{\zeta^{(ret)}\} > \tau_1\{\zeta^{(local)}\}$. Thus, the viscoelastic and dielectric properties for the combined DTD-CR process were calculated from eqs 35−39 together with eq 42, and these calculated properties were compared with the data. The results of this comparison are presented below.

**4.6. Comparison of the DTD-CR Model with Experiments.** Combining the CR relaxation functions for the entanglement segments at $z > z^{**}$ (eqs 35−39 and 42) and the DTD relaxation functions for those at $z < z^{**}$ (eqs 18 and 20), we may incorporate the CR process in the MM model with the tube-edge effect to formulate the viscoelastic $\mu(t)$ and dielectric $\Phi(t)$:

$$\mu(t) = \frac{7}{3L_{eq}}\int_0^{z^{**}}\left[1-\frac{z}{L_{eq}}\right]^{4/3}\exp\left(-\frac{t}{\tau_{MM}(z)}\right)dz + I_{CR,G}\mu_{CR}(t) \qquad (43)$$

$$\Phi(t) = \frac{1}{L_{eq}}\int_0^{z^{**}}[1+\Xi(z)]\exp\left(-\frac{t}{\tau_{MM}(z)}\right)dz + I_{CR,\epsilon}\Phi_{CR}(t) \qquad (44)$$

with

$$\Xi(z) = \frac{1}{6N_a}\left\{\left(1-\frac{z}{L_{eq}}\right)^{-7/3} - \left(1-\frac{z}{L_{eq}}\right)^{-5/3}\right\} \qquad (45)$$

and

$$I_{CR,G} = \left(1-\frac{z^{**}}{L_{eq}}\right)^{7/3},$$
$$I_{CR,\epsilon} = 1 - \frac{z^{**}}{L_{eq}} - \frac{1}{8N_a}\left\{1-\left(1-\frac{z^{**}}{L_{eq}}\right)^{-2/3}\right\}^2 \qquad (46)$$

This modified MM model is hereafter referred to as the DTD-CR model. The fundamental parameters included in this model are $N_a$, $\tau^*$ (the Rouse relaxation time in one entanglement segment), and $z^{**}$ (the DTD-CR threshold): The $\tau^*$ is determined in a way similar to that for the original MM model, and $z^{**}$ is given in Figure 12. The other parameters, $N_{CR}$ and $\zeta_{eff}$, are calculated from $z^{**}$, $\tau_{MM}(z^{**})$ (eq 14), $N_a$, $L_{eq}$, and $\kappa$ ($= 3k_BT/a^2$); see eqs 34 and 42. The CR relaxation times

$\tau_\alpha^{(CR)}$ included in the $\mu_{CR}(t)$ and $\Phi_{CR}(t)$ functions (eqs 35 and 36) are calculated from $N_{CR}$, $\zeta_{eff}$, and $\kappa$; see eqs 38 and 39.

In eqs 43 and 44, the first integration terms indicate the DTD relaxation, and the second terms represent the CR relaxation with the intensities $I_{CR,G}$ and $I_{CR,\epsilon}$ given by eq 46. These intensities, evaluated by subtracting the intensities for the DTD process (the first terms at $t = 0$) from unity, are smaller than the initial memory ($= 1 - z^{**}/L_{eq}$) sustained by the segments at $z > z^{**}$. Thus, in the DTD-CR model, these segments partially relax during the DTD process and fully relaxes during the terminal CR process.

Concerning this point, we note that the mode intensity factors for $\Phi_{CR}$, $\sin^{-2}[p\pi/2N_{CR}]$ (cf. eq 36), rapidly decreases with increasing mode index $p$. Thus, the incorporation of the CR process to $\Phi$ (eq 44) is practically equivalent to a transfer of the dielectric intensity $I_{CR,\epsilon}$ from the terminal DTD relaxation of the MM model to the single-mode CR relaxation occurring at $\tau_2^{(CR)}$.

For the highly entangled PI stars with $N_a = 12$ and 16, the viscoelastic and dielectric properties calculated from the DTD-CR model are shown with the dotted curves in Figures 9 and 10. The $\mu_{CR}$ and $\Phi_{CR}$ terms included in eqs 43 and 44 require $N_{CR}$ to be integer (cf. eqs 35 and 36), but the $N_{CR}$ (eq 34) obtained from $z^{**}$ (Figure 12) was not the integer number. Thus, in the calculation, the $N_{CR}$ was replaced by the closest integer $n_{CR}$ ($= 2$ and 3 for $N_a = 12$ and 16), and the $z^{**}$ value was adjusted accordingly ($z^{**} = L_{eq}(1 - n_{CR}/N_a)$). The $N_a$ values utilized in the calculation were the same as those for the original MM model ($N_{a,cal} = 15$ and/or 20), and the remaining parameter $\tau^*$ was chosen in a way that the $\eta_0$ calculated from the DTD-CR model coincided with the $\eta_0$ data.

In the top panels in Figures 9 and 10, we note that the incorporation of the CR process in the MM model hardly changes the model prediction for the viscoelastic moduli; compare the solid and dotted curves. This result reflects a fact that a large fraction of the initial modulus sustained by the segments at $z > z^{**}$ has relaxed during the DTD process, and only a small intensity $I_{CR,G}$ (eq 46) remains for the CR process of these segments. In other words, the CR process is hardly detected through the viscoelastic moduli.

In contrast, the dielectric behavior is significantly affected by the CR process (because a considerably large dielectric intensity $I_{CR,\epsilon}$ remains for this process); see the middle and bottom panels of Figures 9 and 10. The terminal dielectric relaxation calculated from the DTD-CR model is considerably faster than that deduced from the MM model (with/without tube-edge effect) and appears to be in better agreement with the data; compare the dotted and dashed/solid curves. Specifically, the DTD-CR model (with the chosen $z^{**}$ value; cf. Figure 12) well describes the $\epsilon''/\Delta\epsilon$ peak frequency in the terminal regime.

A comment needs to be added for the DTD-CR model giving this improved description of the dielectric behavior. As explained earlier, the tube-edge effect on $\Phi(t)$ is not negligible at long $t$. Thus, we have incorporated this effect in the model (cf. the $\Xi$ factor in eq 44). However, we can formulate the DTD-CR model without this effect; the $\Phi(t)$ for this case is given by eq 44 with $\Xi(z) = 0$ and $I_{CR,\epsilon} = 1 - z^{**}/L_{eq}$. The height of the terminal $\epsilon''$ peak calculated from this $\Phi(t)$ was a little larger than that in the presence of the tube effect (cf. dotted curves in the bottom panels of Figures 9 and 10), but the terminal relaxation frequency did not change with this effect. Thus, the incorporation of the CR mechanism in the model improved the dielectric description (compared to the original MM model) in either the presence or absence of the tube-edge effect.

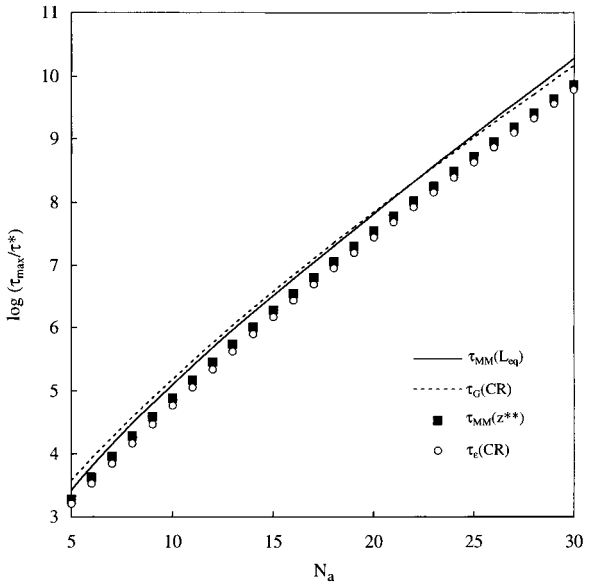


**Figure 14.** $N_a$ dependence of the experimentally detectable longest relaxation time $\tau_{max}$ predicted from the MM and DTD-CR models.

Finally, we compare the *experimentally detectable* longest relaxation time $\tau_{max}$ predicted from the DTD-CR and MM models. Figure 14 shows the $N_a$ dependence of $\tau_{max}$. In the MM model, the terminal relaxation is achieved through the full arm retraction along the dilated tube, and both of the viscoelastically and dielectrically detectable $\tau_{max}$'s coincide with $\tau_{MM}(L_{eq})$.

In the DTD-CR model, the rigorously defined *viscoelastic* $\tau_{max}$ is given by half of the slowest CR eigenmode relaxation time, $\tau_G(CR) = \tau_1^{(CR)}/2$ (cf. eq 35). This $\tau_G(CR)$, evaluated from $z^{**}$ shown in Figure 12, is close to $\tau_{MM}(L_{eq})$. However, the terminal CR mode has a very small viscoelastic intensity $I_{CR,G}$. Thus, the experimentally detectable viscoelastic $\tau_{max}$, that should be close to the measured $\langle\tau_G\rangle_w$ (Figure 6), is decreased to the time $\tau_{MM}(z^{**})$ required for the retraction over the distance $z^{**}$.

The situation is different for the dielectric behavior of the DTD-CR model. Because of the dipole inversion of the PI stars, the slowest CR eigenmode is dielectrically inert. Thus, the dielectrically detectable $\tau_{max}$ (that should be close to the measured $\langle\tau_\epsilon\rangle_w$; cf. Figure 6) coincides with the relaxation time of the second-slowest CR eigenmode, $\tau_\epsilon(CR) = \tau_2^{(CR)}$. As seen in Figure 14, this $\tau_\epsilon(CR)$ is close to the viscoelastic $\tau_{max}$ ($= \tau_{MM}(z^{**})$) but is considerably smaller than $\tau_{MM}(L_{eq})$. This difference between $\tau_\epsilon(CR)$ and $\tau_{MM}(L_{eq})$ is reflected in the acceleration of the terminal dielectric relaxation due to the CR mechanism seen in Figures 9 and 10.

In Figure 14, we also note that the incorporation of the CR process in the MM model decreases the viscoelastic and dielectric $\tau_{max}$ values but hardly changes the exponential $N_a$ dependence of $\tau_{max}$. (Note that the semilogarithmic plots of $\tau_{MM}(z^{**})$, $\tau_\epsilon(CR)$, and $\tau_{MM}(L_{eq})$ have an almost identical slope.) Thus, the DTD-CR model can describe the experimentally observed $N_a$

dependence of $\langle\tau_\epsilon\rangle_w$ and $\langle\tau_G\rangle_w$ (Figure 6) with the accuracy similar to that for the MM model. From this result as well as the moderate improvement in the dielectric prediction due to the incorporation of the CR process (Figures 9 and 10), the combination of the DTD and CR processes appears to be essential for the accurate description of the star chain dynamics.

## 5. Concluding Remarks

For highly entangled PI stars having the type A dipoles in each arm, we have examined the viscoelastic and dielectric properties within the context of the tube model considering the DTD and CR processes. Comparison of these properties indicates that the simplest DTD picture (arm retraction in the fully dilated tube having the diameter $a' = a\{\varphi'(t)\}^{-d/2}$) fails in the dominant part of the terminal relaxation. This result, found irrespective of the tube-edge effect on the dielectric $\Phi(t)$, suggests that the CR mechanism has a significant contribution to the terminal relaxation of the star chains.

On the basis of this result, we have modified the MM model. This modification was made by introducing the DTD-CR crossover threshold $z^{**}$ and simply adding the DTD and CR relaxation functions (the latter being defined only for the entanglement segments at $z > z^{**}$). This crude modification, separately treating the relaxation of the segments at $z > z^{**}$ and $z < z^{**}$, moderately improves the model prediction for the dielectric behavior, while preserving the success for the viscoelastic behavior. This improvement is related to the dielectric extinction of the slowest CR eigenmode due to the dipole inversion at the branching point.

Of course, the real DTD-CR crossover would be gradual (not occurring sharply at $z^{**}$), and the real CR process is not perfectly described by the Rouse−Ham dynamics[2] assumed in the above DTD-CR model. In addition, the distribution of the entanglement lifetime[11] needs to be quantitatively considered in a self-consistent description of the effect of the relaxed segments at $z < z^{**}$ on the terminal CR relaxation of the segments at $z > z^{**}$. (The DTD-CR model considered this effect only in a crude way explained for eqs 40−42.) Furthermore, the experimentally observed failure of the simplest DTD picture may be also related to the other possible relaxation route, the arm retraction in a partially dilated tube (having $a' < a\{\varphi'(t)\}^{-d/2}$).[31] Refinement for these points would improve the model prediction.

The DTD model (MM model) excellently describes the viscoelastic moduli of the PI stars. However, the results presented in this paper demonstrate the importance of the CR mechanism in the accurate description of the arm *motion* underlying all kinds of dynamic properties (including the moduli), thereby suggesting a convincing direction of the model refinement. This refinement, achieved by self-consistent combination of the CR and the full/partial DTD processes, is an important subject of future work.

**Acknowledgment.** The authors thank T. C. B. McLeish for his invaluable comments about this paper. This work was partly supported by the Ministry of Education, Culture, and Sports, Science, and Technology, Japan (Grant 12650884 and 13650952) and by Japan Chemical Innovation Institute (through the Doi Project for development of Platform for designing high functional materials). Y.M. acknowledges, with thanks, financial support from JSPS Research Fellowship for Young Scientist.

## Appendix A. Evaluation and Use of Dielectric Spectrum

**A-1. Iteration Method for Evaluation of Spectrum.** In calculation of the dielectric spectrum with the iteration method,[16] we assumed a semicontinuous distribution of the dielectric relaxation times having a small logarithmic span, $\log[\tau_p/\tau_{p+1}] = \Delta$ with $\Delta \le 0.2$, and determined the dielectric intensities $g_p$ that reproduced the normalized $\epsilon''/\Delta\epsilon$ data (written in terms of $\tau_p$ and $g_p$; cf. eq 7).

As a first estimate of $g_p$, we chose $g_p^{(1)} = 0.5\pi\{\epsilon''(\omega = 1/\tau_p)/\Delta\epsilon\}_{obs}$ suggested from the crudest approximation for the spectrum.[1] (Hereafter, the superscript enclosed in parentheses denotes the number of iterated calculation cycles.) The $\{\epsilon''(\omega)/\Delta\epsilon\}_{calc}^{(1)}$ values calculated from the first set of $g_p^{(1)}$ and $\tau_p$ were obviously different from the $\epsilon''(\omega)/\Delta\epsilon$ data. Thus, we introduced the convergence factor for $g_p^{(1)}$:

$$C_p^{(1)} = \left(\frac{\{\epsilon''(\omega=1/\tau_p)/\Delta\epsilon\}_{obs}}{\{\epsilon''(\omega=1/\tau_p)/\Delta\epsilon\}_{calc}^{(1)}}\right)^{\delta} \tag{A1}$$

Here, the exponent $\delta$ adjusts a rate of the convergence and a magnitude of oscillation in the calculation. This $\delta$ value was chosen to be 0.4−0.7. Utilizing this $C_p^{(1)}$ factor, we evaluated the intensity in the second cycle of iteration as $g_p^{(2)} = C_p^{(1)} g_p^{(1)}$.

The calculation cycles were iterated in this way, with the convergence factor $C_p^{(n)}$ being recalculated at the end of each cycle. After the iteration over 30 cycles, the difference between the calculated and measured $\epsilon''/\Delta\epsilon$, averaged over the entire range of $\omega$, became less than 0.01%, which was much smaller than the experimental uncertainties in the $\epsilon''/\Delta\epsilon$ data. Thus, we utilized the $g_p^{(30)}$ values as the dielectric intensities to calculate $G^*/G_N$ for the DTD process (cf. eq 30).

The $\epsilon''/\Delta\epsilon$ and $\{\epsilon_0 - \epsilon'\}/\Delta\epsilon$ data were reproduced with equally high accuracies from the spectra $\{g_p^{(30)}, \tau_p\}$ with different $\Delta$ values ($\le$0.2). This nonuniqueness is well-known for the empirical determination of semicontinuous spectra. However, the nonuniqueness did not disturb our test of the DTD relationship because the spectra with $\Delta \le 0.2$ gave indistinguishable $G^*/G_N$ values for the DTD process. Thus, in Figures 7 and 8, we utilized the $G^*/G_N$ calculated for $\Delta = 0.1$.

**A.2. Use of Dielectric Spectrum in the Test of DTD.** In principle, the test of the DTD picture does not require the explicit evaluation of the dielectric spectrum: We can directly obtain the $\Phi(t)$ value as a function of $t$ via the numerical, inverse Fourier transformation of the $\epsilon''/\Delta\epsilon$ data (cf. eq 5). Then, the moduli for the DTD process can be numerically calculated as the Fourier transformation of $\mu_{DTD} = [\Phi(t)]^{1+d}$ (cf. eq 2). However, this straightforward method required a long calculation time (for the numerical transformation in two steps). Thus, we utilized the dielectric spectrum to calculate the moduli in a semianalytic way (eq 30). In this sense, the use of the spectrum in the test of the DTD picture is just for convenience of calculation.

A further comment needs to be added for the dielectric spectrum itself. In description of the slow entanglement dynamics, we often choose the entanglement segment

as the motional unit. Then, in a discretized expression, $\Phi(t)$ of a chain composed of $N$ entanglement segments is contributed from $N$ modes. In contrast, in this paper, we evaluated the spectrum in a semicontinuous sense: Namely, we introduced more than $N$ modes (with $\tau_p$ being narrowly spanned in the logarithmic scale) to evaluate their intensities $g_p$ with the method explained in Appendix A.1.

Since the test of the DTD picture just requires the $\Phi(t)$ value, we can safely use this semicontinuous spectrum instead of the discretized $N$-mode spectrum, as long as the former spectrum reproduces the $\epsilon''(\omega)$ and $\Phi(t)$ data with a high accuracy (e.g., with a difference less than 0.01%). This was the case for the spectra utilized in this paper.

**A.3. Additional Comment for the Spectrum.** One of the reviewers for this paper focused on the nonsinusoidal form of the dielectric eigenfunctions of linear chains[2,14,32−35] to pose a question about the expression of the dielectric $\Phi(t)$ given by a sum of exponentially decaying modes (eq 6). However, this expression is derived irrespective of the functional form of the eigenfunctions, as explained below.

For a linear chain composed of $N$ entanglement segments, a local correlation function $C(n,t;n')$ is defined in terms of the bond vector $\mathbf{u}(n,t)$ of $n$th entanglement segment at the time $t$:[2,14,32]

$$C(n,t;n') = \frac{1}{a^2}\langle \mathbf{u}(n,t)\cdot\mathbf{u}(n',0)\rangle \quad (a^2 = \langle \mathbf{u}^2\rangle) \quad \text{(A2)}$$

This $C(n,t;n')$ can be expanded into its eigenmodes as[2,14,28,32,35]

$$C(n,t;n') = \frac{2}{N}\sum_{p=1}^{N} f_p(n)\, f_p(n') \exp\left(-\frac{t}{\tau_p}\right) \quad \text{(A3)}$$

where $f_p$ and $\tau_p$ are the eigenfunction and relaxation time of the $p$th eigenmode.

For the type A linear chain, $\Phi(t)$ is given by an integral of $C(n,t;n')$ with respect to $n$ and $n'$.[2,14] Specifically, for the chain without dipole inversion (i.e., the linear PI examined in this paper), $\Phi(t)$ is written as[2,14,32−35]

$$\Phi(t) = \sum_{p\geq 1} g_p \exp\left(-\frac{t}{\tau_p}\right) \quad \text{with } g_p = \frac{2}{N^2}\left[\int_0^N f_p(n)\, \mathrm{d}n\right]^2 \quad \text{(A4)}$$

Experiments[32−35] revealed the nonsinusoidal $n$ dependence of $f_p(n)$ for the PI chains in concentrated systems. However, eq A4 clearly indicates that $\Phi(t)$ is expressed as a sum of the exponentially decaying modes irrespective of the $n$ dependence of $f_p(n)$: A change in the functional form of $f_p(n)$ results in a change of the dielectric mode distribution (through a change of $g_p$; cf. eq A4) but *never* affects the exponentially decaying feature of $\Phi(t)$ itself. (In refs 28 and 32−35, further explanations are presented for the validity of the eigenmode expansion of $C(n,t;n')$ and the molecular origin of the nonsinusoidal form of $f_p(n)$.)

## Appendix B. Test of DTD Criteria in the Absence of Tube-Edge Effect

For the tube to dynamically dilates to the diameter $a'$, successive $(a'/a)^2$ entanglement segments of the chain need to be mutually equilibrated through their CR motion.[2,10] In a largely dilated tube, this equilibration requires a time $\tau^{**} = f(a'/a)^4 t_w$ (a continuous Rouse-CR expression of $\tau^{**}$),[2,10,11] where $t_w$ is the local entanglement lifetime[24] and $f$ is a numerical prefactor.[11]

If the entanglement lifetime is broadly distributed (for the case of star chains), the $t_w$ for the terminal CR process is to be redefined as an effective CR time unit $t_{w,eff}$ that determines the large-scale CR equilibration time, $\tau^{**} = f(a'/a)^4 t_{w,eff}$. In the terminal regime, the lifetime distribution would be averaged/smeared so that we may utilize this functional form of $\tau^{**}$ characterized by the single $t_{w,eff}$.[11]

On the basis of the above argument, the $t_w$ and $f$ were evaluated with a previously explained method.[11] For the linear chains having a narrow distribution of the entanglement lifetime, the Graessley model[24] formulated on the basis of the single $t_w$ (defined in a way explained for eq 32) was utilized in the evaluation. The results are $f = 4/\pi^2$ and $t_w = (\pi^2/12)^{n_g}\tau_\epsilon/n_g = 0.11\tau_\epsilon$,[36] where $\tau_\epsilon$ is the longest dielectric relaxation time that can be replaced by the $\langle\tau_\epsilon\rangle_w$ data (Figure 6), and $n_g$ ($\cong$4 for *linear* PI)[37] is a number of constraints per each entanglement point.[24]

For the star chains with $N_a \leq 6$, experiments indicated that the terminal relaxation time is close to the global CR relaxation time.[2,38] A relationship deduced from this result, $ft_{w,eff} = \tau_\epsilon/N_a^2 \cong \langle\tau_\epsilon\rangle_w/N_a^2$,[11] was extended to highly entangled PI stars to evaluate the product $ft_{w,eff}$. Since this product was evaluated from the terminal time $\langle\tau_\epsilon\rangle_w$, the $t_{w,eff}$ included in this product is to be regarded as the effective CR time unit averaged over the lifetime distribution in the terminal regime of the star chains.

The DTD criterion, $t > \tau^{**} = f(a'/a)^4 t_w$, can be quantitatively examined with the $f$ and $t_w$ (or $t_{w,eff}$) values thus obtained. In the time scale where this criterion is satisfied, the dilated tube diameter is expressed as $a' = a\{\Phi(t)\}^{-d/2}$ (in the absence of the tube-edge effect). The $a'/a$ ratio is the smallest for $d = 1$, and the corresponding (most easily satisfied) criterion can be cast in a form[11]

$$\Phi(t) \geq \left\{\frac{ft_w}{t}\right\}^{1/2} \quad (\text{for } d = 1) \quad \text{(B1)}$$

An additional criterion, requiring the chain size to be smaller than the dilated tube diameter, is written as[11]

$$\Phi(t) \geq 1/N \text{ (for linear chains)}, \quad 1/N_a \text{ (for star chains)} \quad \text{(B2)}$$

Figure 15 tests the validity of eqs B1 and B2 for the highly entangled star PI ($N_a = 12$) and linear PI ($N = 62$) having almost identical $\langle\tau_\epsilon\rangle_w$ (cf. Figure 6). The circles indicate the $\Phi(t)$ evaluated from the dielectric spectra data (cf. Appendix A.1), the solid lines represent the $\{ft_{w,eff}/t\}^{1/2}$ and/or $\{ft_w/t\}^{1/2}$ factor, and the dotted lines show the $1/N$ and/or $1/N_a$ factor. For the star PI, $\Phi(t)$ is smaller than $\{ft_{w,eff}/t\}^{1/2}$, and the DTD criterion (eq B1) is violated in the dominant part of the terminal regime. In contrast, eqs B1 and B2 are satisfied for the linear PI at long $t > 0.1\tau_\epsilon$. These results are in harmony with the failure and success of the DTD relationship between the viscoelastic and dielectric data (cf. Figures 7 and 8).

Figure 15 also demonstrates why the DTD picture is valid for the linear PI but fails for the star PI. The linear

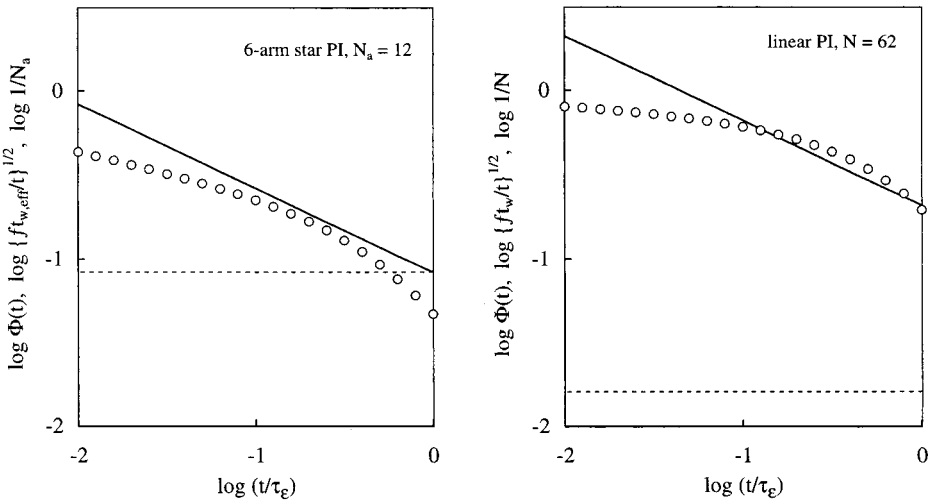


**Figure 15.** Test of the DTD criteria (in absence of the tube-edge effect) for highly entangled star and linear PI chains having nearly the same longest dielectric relaxation time $\tau_\epsilon$. The criteria are satisfied if $\Phi(t)$ (circles) is larger than $\{ft_w/t\}^{1/2}$ (solid line) and $1/N_a$ or $1/N$ (dotted line). For further details, see Appendix B.

PI has a narrow dielectric mode distribution so that its $\Phi(t)$ does not significantly decay at $t \leq \tau_\epsilon$. This behavior of $\Phi(t)$ allows the DTD criteria to be satisfied at long $t$ (despite a fact that the $\{ft_w/t\}^{1/2}$ factor has a relatively large value even at $t = \tau_\epsilon$). In contrast, the PI star has a significantly broad dielectric mode distribution, thereby exhibiting considerably small $\Phi(t)$ ($<\{ft_{w,eff}/t\}^{1/2}$) at long $t$.

Within the context of the DTD-CR model, we can compare the above DTD criterion (eq B1) with the criterion formulated on the basis of eq 33. In this model, the terminal dielectric relaxation of the dipole-inverted star chain corresponds to the second-slowest CR eigenmode, and the $ft_{w,eff}$ factor ($=\tau_\epsilon/N_a^2$) is given by (cf. eqs 39 and 42)

$$ft_{w,eff} = \frac{4\sin^2\left(\frac{\pi}{2(2N_{CR}+1)}\right)}{N_a^2 \sin^2\left(\frac{\pi}{2N_{CR}}\right)}\tau_{MM}(z^{**}) \cong \frac{\tau_{MM}(z^{**})}{N_a^2} \quad \text{for } N_{CR} \geq 2 \quad \text{(B3)}$$

From this factor, we evaluated the CR equilibration time used in eq B1, $\tau^{**}(z) = f(a'(z)/a)^4 t_{w,eff}$. For large $z$, this $\tau^{**}(z)$ was found to be smaller than the $\tau^{**}(z)$ given by eq 33, meaning that the test of the DTD criterion based on eq 33 (Figure 12) is more severe than the test made in Figure 15.

## Appendix C. Viscoelastic and Dielectric Features of BM and MM Models

**C.1. Validity of DTD Relationship.** For convenience of the detailed test of the DTD picture within the context of the tube model, this section summarizes the viscoelastic and dielectric features of the BM and MM models in absence of the tube-edge effect.

The $\mu(t)$ of the BM and MM models is given by eq 18. The $\Phi(t)$ formulated for these models is given by eq 20 with $\Xi = 0$, $z_c = L_{eq}$, and $K_n = 1$. For a star with $N_a = 15$, Figure 16 shows plots of these $\mu(t)$ and $\Phi(t)$ against a reduced time $t/\tau_{arm}$. Here, $\tau_{arm}$ denotes the longest relaxation time deduced from the models; $\tau_{arm} = \tau_{BM}(L_{eq})$ and/or $\tau_{MM}(L_{eq})$ (cf. eqs 13 and 14).

For these models, we here test the validity of the simplest DTD relationship, $\mu(t) = [\Phi(t)]^{1+d}$ (eq 2).

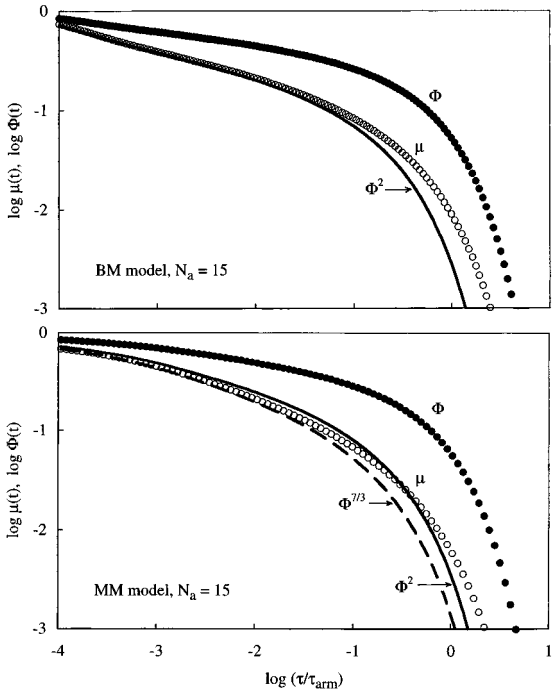


**Figure 16.** Plots of $\mu(t)$ and $\Phi(t)$ of BM model (top panel) and MM model (bottom panel) against a reduced time $t/\tau_{arm}$ ($\tau_{arm}$ = longest relaxation time deduced from the models). The solid and dashed curves indicate plots of $[\Phi(t)]^2$ and $[\Phi(t)]^{7/3}$, respectively.

Utilizing this relationship, we calculated $\mu(t)$ from the $\Phi_{BM}(t)$ and $\Phi_{MM}(t)$ of the BM and MM models. The result are shown in Figure 16 with the solid curve (in the top panel; $d = 1$ for the BM model) and dashed curve (in the bottom panel; $d = {}^4/_3$ for the BM model). At short $t$, these curves agree with the $\mu_{BM}(t)$ and $\mu_{MM}(t)$ of the models directly calculated from eq 18 (unfilled circles). However, a deviation is observed at long $t$ (in a vicinity of $\tau_{arm}$), meaning that the simplest DTD relationship does not hold for the BM/MM models at long $t$. This deviation reflects a fact that the simplest DTD relationship is derived from the analysis of the *average* tube survival fraction $\varphi'$ while the BM/MM models are formulated on the basis of the *conditional* tube survival fraction, $\tilde{\varphi}' = 1 - z/L_{eq}$ defined for a given retraction distance $z$.

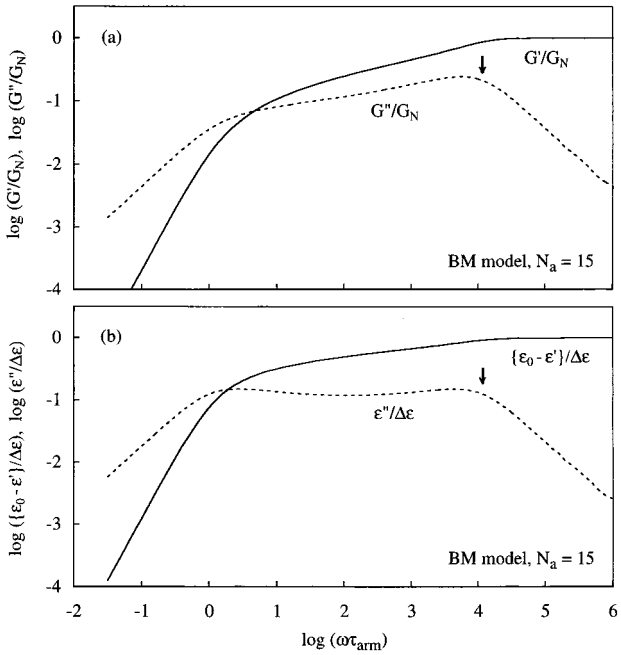


**Figure 17.** Normalized viscoelastic and dielectric properties, $G'/G_N$ and $G''/G_N$ (top panel) and $\{\epsilon_0 - \epsilon'\}/\Delta\epsilon$ and $\epsilon''/\Delta\epsilon$ (bottom panel), calculated from the BM model. The thick arrows indicate a high-frequency cutoff ($1/\tau^*$) of the model.

From the above result, one might argue that the observed failure of the simplest DTD relationship (Figure 7) does not indicate the failure of the BM/MM models. However, Figures 9−11 clearly demonstrate that the models excellently describe the viscoelastic data, but considerable differences exist for the dielectric data. This result indicates a necessity of modification of the models (through explicit incorporation of the CR process).

In addition, the $\mu_{MM}(t)$ of the MM model (unfilled circles in the bottom panel of Figure 16) is numerically close to $[\Phi_{MM}(t)]^2$ (solid curve) in the entire range of $t \leq \tau_{arm}$. Namely, in absence of the tube-edge effect, the simplest DTD relationship with $d = 1$ holds for the MM model as a good approximation (although the intrinsic $d$ value of this model is $^4/_3$). This approximate validity of the DTD relationship with $d = 1$ was confirmed for the MM model in a wide range of $N_a$ between 5 and 30. Thus, the failure of this relationship (Figure 7) is almost equivalent to the deviation of the MM prediction from the dielectric data (Figures 9 and 10).

Here, a comment is added for the MM model in the presence of the tube-edge effect. For this case, $\mu_{MM}(t)$ was found to be numerically close to $[\Phi_{MM}(t)]^{7/3}$ (with $\Phi_{MM}(t)$ being calculate from eqs 20 and 21). Thus, the DTD relationship with the intrinsic $d$ value holds for the MM model as a good approximation in the presence of the tube-edge effect.

**C.2. Comparison of BM and MM Models.** Figures 17 and 18 respectively show the normalized dynamic moduli ($G'/G_N$ and $G''/G_N$) and dielectric properties ($\{\epsilon_0 - \epsilon'\}/\Delta\epsilon$ and $\epsilon''/\Delta\epsilon$) of the BM and MM models in absence of the tube-edge effect. These normalized quantities are plotted against a reduced frequency $\omega\tau_{arm}$. For the BM and MM models, a single peak is observed for $G''/G_N$ and broad double peaks are noted for $\epsilon''/\Delta\epsilon$. For both models, the terminal $\epsilon''/\Delta\epsilon$ peak seen at $\omega\tau_{arm} = 1$ corresponds to the full retraction of the arm in the dilated tube. However, the origin of the high-$\omega$ peaks of $\epsilon''/\Delta\epsilon$ and $G''/G_N$ is different in the two models.

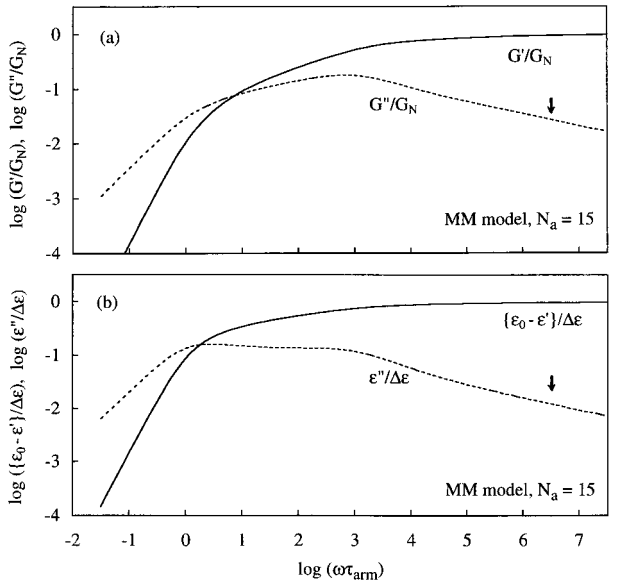


**Figure 18.** Normalized viscoelastic and dielectric properties, $G'/G_N$ and $G''/G_N$ (top panel) and $\{\epsilon_0 - \epsilon'\}/\Delta\epsilon$ and $\epsilon''/\Delta\epsilon$ (bottom panel), calculated from the MM model. The thick arrows indicate a high-frequency cutoff ($1/\tau^*$) of the model.

For the BM model, these high-$\omega$ peaks are observed at a frequency $1/\tau^*$ (thick arrow in Figure 17), where $\tau^*$ is the Rouse relaxation time in one entanglement segment. This $\tau^*$ is introduced in the model as the smallest unit of time (i.e., short-time cutoff). Thus, the peaks seen at $\omega = 1/\tau^*$ indicate a high-frequency cutoff of the model and have no significant physical meaning. Consequently, the $\epsilon''/\Delta\epsilon$ and $G''/G_N$ peaks of the highly entangled PI star, attributable to the Rouse fluctuation of the arm length, are not well described by the BM model; cf. Figure 11. Of course, the BM model focuses on the terminal relaxation, and the lack of the fluctuation mechanism should not be regarded as a flaw in the model.

For the MM model considering the arm length fluctuation, the high-$\omega$ peaks of $\epsilon''/\Delta\epsilon$ and $G''/G_N$ reflect this fluctuation and are observed at $\omega \ll 1/\tau^*$ (thick arrow in Figure 18). Thus, the MM model fairly well describes the fluctuation peaks in the $\epsilon''/\Delta\epsilon$ and $G''/G_N$ data for the PI stars; cf. Figures 9 and 10.

## References and Notes

(1) Ferry, J. D. *Viscoelastic Properties of Polymers*, 3rd ed.; Wiley: New York, 1980.
(2) Watanabe, H. *Prog. Polym. Sci.* **1999**, *24*, 1253.
(3) Doi, M.; Kuzuu, N. *J. Polym. Sci., Polym. Lett. Ed.* **1980**, *18*, 775.
(4) Pearson, D. S.; Helfand, E. *Macromolecules* **1984**, *17*, 888.
(5) Ball, R. C.; McLeish, T. C. B. *Macromolecules* **1989**, *22*, 1911.
(6) Milner, S. T.; McLeish, T. C. B. *Macromolecules* **1997**, *30*, 2159.
(7) Milner, S. T.; McLeish, T. C. B. *Macromolecules* **1998**, *31*, 7479.
(8) Colby, R. H.; Rubinstein, M. *Macromolecules* **1990**, *23*, 2753.
(9) Doi M.; Edwards, S. F. *The Theory of Polymer Dynamics*; Clarendon: Oxford, 1986.
(10) Watanabe, H.; Matsumiya, Y.; Osaki, K. *J. Polym. Sci., Part B: Polym. Phys.* **2000**, *38*, 1024.
(11) Matsumiya, Y.; Watanabe, H. *Macromolecules* **2001**, *34*, 5702.
(12) Stockmayer, W. H. *Pure Appl. Chem.* **1967**, *15*, 539.
(13) Riande, E.; Saiz, E. *Dipole Moments and Birefringence of Polymers*; Prentice Hall: Englewood Cliffs, NJ, 1992.
(14) Watanabe, H. *Macromol. Rapid Commun.* **2001**, *22*, 127.
(15) Matsumiya, Y.; Watanabe, H.; Osaki, K. *Macromolecules* **2000**, *33*, 499.

(16) Yoshida, H.; Adachi, K.; Watanabe, H.; Kotaka, T. *Polym. J.* **1989**, *21*, 863.
(17) Hayakawa, R.; Kanda, H.; Sakamoto, M.; Wada, Y. *Jpn. J. Appl. Phys.* **1975**, *14*, 2039.
(18) Adachi, K.; Hirano, H. *Macromolecules* **1998**, *31*, 3958.
(19) Imanishi, Y.; Adachi, K.; Kotaka, T. *J. Chem. Phys.* **1988**, *21*, 157.
(20) Adachi, K.; Yoshida, H.; Fukui, F.; Kotaka, T. *Macromolecules* **1990**, *23*, 3138.
(21) Some of the $\langle\tau_\epsilon\rangle_w$ and $\langle\tau_G\rangle_w$ data for the low-$M$ linear PI chains (with $M \leq 10^4$) shown in Figure 6 are the data reported by Adachi et al.[19,20] Their definition of $\langle\tau_\epsilon\rangle_w$ and $\langle\tau_G\rangle_w$ was different from that given by eqs 28 and 29. However, the $\langle\tau_\epsilon\rangle_w$ and $\langle\tau_G\rangle_w$ values for those low-$M$ linear PI chains were not significantly affected by this difference.
(22) Fetters, L. J.; Kiss, A. D.; Pearson, D. S.; Quack, G. F.; Vitus, F. J. *Macromolecules* **1993**, *26*, 1647.
(23) Watanabe, H. *Korea-Australia Rheol. J.* **2001**, *13*, 205.
(24) Graessley, W. W. *Adv. Polym. Sci.* **1982**, *47*, 68.
(25) Ham, J. S. *J. Chem. Phys.* **1957**, *26*, 625.
(26) Watanabe, H.; Yoshida, H.; Kotaka, T. *Polym. J.* **1990**, *22*, 153.
(27) The spring forces of the $q$ arms acting on the frictionless branching point are required to be balanced.[25,26] This balance results in the completely antisymmetric (odd) and symmetric (even) eigenmodes.
(28) Watanabe, H.; Yao, M. L.; Osaki, K. *Macromolecules* **1996**, *29*, 97.
(29) Watanabe, H.; Matsumiya, Y.; Osaki, K.; Yao, M. L. *Macromolecules* **1998**, *31*, 7538.
(30) McLeish, T. C. B.; Larson, R. G. *J. Rheol.* **1998**, *42*, 81.
(31) McLeish, T. C. B., private communication.
(32) Watanabe, H.; Urakawa, O.; Kotaka, T. *Macromolecules* **1993**, *26*, 5073.
(33) Watanabe, H.; Urakawa, O.; Kotaka, T. *Macromolecules* **1994**, *27*, 3525.
(34) Watanabe, H.; Yamada, H.; Urakawa, O. *Macromolecules* **1995**, *28*, 6443.
(35) Matsumiya, Y.; Watanabe, H.; Osaki, K.; Yao, M. L. *Macromolecules* **1998**, *31*, 7528.
(36) (a) The Graessley model[24] considers the local CR jump of a probe chain due to pure reptation of the surrounding linear chains (matrix chains). For the actual CR processes, this matrix reptation time should be replaced by the matrix relaxation time $\tau_{mat}$ that is affected by the CR and contour length fluctuation (CLF)[9] mechanisms. (For highly entangled linear chains, the DTD mechanism would not affect $\tau_{mat}$, as suggested from the model by Viovy et al.[36b]) However, the correction of $\tau_{mat}$ due to the CR and CLF effects was found to be minor (less than 15% for the linear PI chains with $N =$ 32 and 64). Thus, for these PI chains, we may safely utilize the $\langle\tau_\epsilon\rangle_w$ data as the longest $\tau_\epsilon$ included in the $t_w$ expression of the Graessley model[24] ($t_w = (\pi^2/12)^{n_s}\tau_\epsilon/n_g$). (b) Viovy, J. L.; Rubinstein, M.; Colby, R. H. *Macromolecules* **1991**, *24*, 3587.
(37) Adachi, K.; Itoh, S.; Nishi, I.; Kotaka, T. *Macromolecules* **1990**, *23*, 2554.
(38) Watanabe, H.; Yoshida, H.; Kotaka, T. *Macromolecules* **1992**, *25*, 2442.

MA011782Z